COMMUNICATIONS PHYSICS

ARTICLE

https://doi.org/10.1038/s42005-020-00448-5 OPEN

Quantum-critical scale invariance in a transition metal alloy

Yasuyuki Nakajima[1,2]✉, Tristin Metz[2], Christopher Eckberg[2], Kevin Kirshenbaum[2], Alex Hughes[2], Renxiong Wang[2], Limin Wang[2], Shanta R. Saha[2], I-Lin Liu[2,3,4], Nicholas P. Butch[2,4], Daniel Campbell[2], Yun Suk Eo[2], David Graf[5], Zhonghao Liu[6,7], Sergey V. Borisenko[6], Peter Y. Zavalij[8] & Johnpierre Paglione[2,9]✉

Quantum-mechanical fluctuations between competing phases induce exotic collective excitations that exhibit anomalous behavior in transport and thermodynamic properties, and are often intimately linked to the appearance of unconventional Cooper pairing. High-temperature superconductivity, however, makes it difficult to assess the role of quantum-critical fluctuations in shaping anomalous finite-temperature physical properties. Here we report temperature-field scale invariance of non-Fermi liquid thermodynamic, transport, and Hall quantities in a non-superconducting iron-pnictide, $Ba(Fe_{1/3}Co_{1/3}Ni_{1/3})_2As_2$, indicative of quantum criticality at zero temperature and applied magnetic field. Beyond a linear-in-temperature resistivity, the hallmark signature of strong quasiparticle scattering, we find a scattering rate that obeys a universal scaling relation between temperature and applied magnetic fields down to the lowest energy scales. Together with the dominance of hole-like carriers close to the zero-temperature and zero-field limits, the scale invariance, isotropic field response, and lack of applied pressure sensitivity suggests a unique quantum critical system unhindered by a pairing instability.

[1] Department of Physics, University of Central Florida, Orlando, FL 32816, USA. [2] Maryland Quantum Materials Center, Department of Physics, University of Maryland, College Park, MD 20742, USA. [3] Chemical Physics Department, University of Maryland, College Park, MD 20742, USA. [4] NIST Center for Neutron Research, National Institute of Standards and Technology, Gaithersburg, MD 20899, USA. [5] National High Magnetic Field Laboratory, Florida State University, Tallahassee, FL 32310, USA. [6] IFW-Dresden, Helmholtzstraße 20, 01069 Dresden, Germany. [7] Shanghai Institute of Microsystem and Information Technology, Chinese Academy of Sciences, Shanghai 200050, China. [8] Department of Chemistry, University of Maryland, College Park, MD 20742, USA. [9] The Canadian Institute for Advanced Research, Toronto M5G 1Z8 ON, Canada. ✉email: yasuyuki.nakajima@ucf.edu; paglione@umd.edu

Non-Fermi liquid (NFL) behavior ubiquitously appears in iron-based high-temperature superconductors with a novel type of superconducting pairing symmetry driven by interband repulsion[1, 2]. The putative pairing mechanism is thought to be associated with the temperature-doping phase diagram, bearing striking resemblance to cuprate and heavy-fermion superconductors[3, 4]. In iron-based superconductors, the superconducting phase appears to be centered around the point of suppression of antiferromagnetic (AFM) and orthorhombic structural order[1]. Close to the boundary between AFM order and superconductivity, the exotic metallic regime emerges in the normal state. The "strange" metallic behavior seems to be universal in strongly correlated metals near a quantum critical point (QCP), characterized by linear-in-T resistivity[5–8]. The universal transport behavior is known as Planckian dissipation, where the transport scattering rate is constrained by thermal energy, $\hbar/\tau_P = k_B T$, where $\hbar$ is the reduced Planck constant and k_B is the Boltzmann constant. Lacking an intrinsic energy scale, the scale-invariant transport in strange metals is one of the unresolved phenomena in condensed matter physics, but its microscopic origin has yet to be fully understood. In iron-based superconductors, along with the AFM order, the presence of an electronic nematic phase above the structural transition complicates the understanding of the superconductivity and NFL behavior[9–12]. Moreover, the robust superconducting phase prohibits investigations of zero-temperature limit normal state physical properties associated with the quantum critical (QC) instability due to the extremely high upper critical fields.

While AFM spin fluctuations are widely believed to provide the pairing glue in the iron pnictides, other magnetic interactions are prevalent in closely related materials, such as the cobalt-based oxypnictides LaCoOX (X = P, As)[13], which exhibit ferromagnetic (FM) orders, and Co-based intermetallic arsenides with coexisting FM and AFM spin correlations[14–16]. For instance, a strongly enhanced Wilson ratio R_W of ~7–10 at 2 K (ref. [17]) and violation of the Koringa law[14–16] suggest proximity to a FM instability in $BaCo_2As_2$. $BaNi_2As_2$, on the other hand, seems to be devoid of magnetic order[18] and rather hosts other ordering instabilities in both structure and charge[19]. Confirmed by extensive study, Fe, Co, and Ni have the same 2+ oxidation state in the tetragonal $ThCr_2Si_2$ structure, thus adding one d electron (hole) contribution by Ni (Fe) substitution for Co in $BaCo_2As_2$ (refs. [20–23]), and thereby modifying the electronic structure subtly, but significantly enough to tune in and out of different ground states and correlation types. Utilizing this balance, counter-doping a system to achieve the same nominal d electron count as $BaCo_2As_2$ can realize a unique route to the same nearly FM system, while disrupting any specific spin correlation in the system.

Here, we utilize this approach to stabilize a novel ground state in the counter-doped nonsuperconducting iron pnictide $Ba(Fe_{1/3}Co_{1/3}Ni_{1/3})_2As_2$, also nearly FM but with a unique type of spin fluctuation that leads to very strong quasiparticle scattering. We show that NFL behavior is prevalent in the very low-temperature charge transport and thermodynamic properties of $Ba(Fe_{1/3}Co_{1/3}Ni_{1/3})_2As_2$, with temperature and magnetic energy scale invariance arising from a QC ground state.

Results

Non-Fermi liquid magnetotransport. The hallmark of NFL behavior in $Ba(Fe_{1/3}Co_{1/3}Ni_{1/3})_2As_2$ is clearly observed in the resistivity (Fig. 1a), which exhibits a quasi-linear T dependence over three orders of magnitude variation, from 20 K down to at least 20 mK at $B = 0$ T. In this temperature range, we find no discernible anomaly associated with phase transitions down to 20 mK, suggestive of the realization of an anomalous metallic ground state that persists to the $T = 0$ limit. Furthermore, this behavior is strongly suppressed with magnetic field, which drives a recovery of Fermi liquid (FL) behavior (i.e., $\rho \propto T^2$) at low temperatures (Supplementary Note 1).

Note that the unusual resistivity observed in $Ba(Fe_{1/3}Co_{1/3}Ni_{1/3})_2As_2$ cannot be ascribed to either Mooij correlations[24] or quantum interference[25] due to randomness introduced by counter-doping. Given that the Mooij correlations are dominant, increasing randomness enhances the residual resistivity ρ_0, accompanied by a gradual change in the slope of $\rho(T)$ at high temperatures, as observed in $LuRh_4B_4$ (ref. [25]). However, the overall slope of resistivity in $Ba(Fe_{1/3}Co_{1/3}Ni_{1/3})_2As_2$ is parallel shifted from that in $BaCo_2As_2$ with a sizable increase of residual resistivity by ~30 μΩ cm, indicative of the absence of Mooij correlation (Supplementary Note 2). Also, the quasi-T-linear dependence of the resistivity at low temperatures in $Ba(Fe_{1/3}Co_{1/3}Ni_{1/3})_2As_2$ cannot be reproduced by the quantum corrections in conductivity caused by interference that provide the power law $\sigma \sim T^{p/2}$ (or $\rho \sim T^{-p/2}$), where $p = 3/2$ (dirty limit), 3 (electron–phonon scattering), or 1 (enhanced electron–electron interaction)[25]. The absence of Mooij correlations and quantum interference allows us to treat scattering sources in charge transport independently. As demonstrated by a smooth change in the temperature slope of resistivity at ~30 K (Supplementary Fig. 2), the inelastic scattering dominates over the electron–phonon scattering in the charge transport at low temperatures.

Mimicking the quasi-linear behavior in the temperature dependence of $\Delta\rho(T) = \rho(T) - \rho(0)$ at 0 T (Fig. 1a inset), the magnetoresistance (MR) at 1.31 K $\Delta R(B)/R(0)$ varies sublinearly with applied field up to 35 T (Fig. 1b). The quasi-linear T and B dependence allow us to introduce a new energy scale involving the scattering rate, the quadrature sum of temperature and magnetic field $\Gamma(T, B) \equiv \sqrt{(k_B T)^2 + (\eta \mu_B B)^2}$, where μ_B is the Bohr magneton and η is a dimensionless parameter. Here, we treat η as a fitting parameter rather than a value extracted from other measurements or microscopic theoretical calculations. Setting $\eta = 0.67$, we find the unusual scaling in the inelastic scattering rate, $\hbar/\tau = \hbar n e^2(\rho(T, B) - \rho(0, 0))/m^*$, where n is the carrier density extracted from low-temperature Hall coefficient measured at 0.5 T and m^* is the effective mass obtained from low-temperature-specific heat measured at 10 T in the present work, as a function of $\Gamma(T, B)$, collapsing onto one universal curve as shown in Fig. 1c. This scaling is reminiscent of the observation in QC iron pnictide $BaFe_2(As,P)_2$ (ref. [5]). Although $Ba(Fe_{1/3}Co_{1/3}Ni_{1/3})_2As_2$ and $BaFe_2(As,P)_2$ share the similar scaling relation in magnetotransport with each other, we note that while the scaling relation holds in the high Γ region above ~3 meV in $BaFe_2(As,P)_2$, it holds in the low Γ region below ~2 meV in $Ba(Fe_{1/3}Co_{1/3}Ni_{1/3})_2As_2$, and that the extracted value of dimensionless parameter η (γ/α in ref. [5]) is different from that reported in ref. [5].

The $\Gamma(T, B)$ scaling can closely be correlated to the Planckian bound of dissipation. Quantum mechanics allows the shortest dissipative time scale $\tau_P = \hbar/k_B T$, constrained by the uncertainty principle between dissipative time scale τ and energy dissipation $E \sim k_B T$, $\tau \cdot k_B T \gtrsim \hbar$. Redefining $\Gamma(T, B)$ as the dissipation energy scale in magnetic field, we can obtain the universal bound of dissipation, $\hbar/\tau_P \sim \Gamma(T, B)$. Our experimental observation in $\Gamma(T, B)$ scaling for the inelastic scattering gives a linear relation, $\hbar/\tau = A\Gamma(T, B)$ with $A = 1.80$, in good agreement with expected behavior.

Notwithstanding the quasi-two-dimensional layered structure, the NFL magnetotransport is independent of applied field orientations with respect to the FeAs layers. We plot the anisotropy of the MR, $\Delta\rho(B \parallel c)/\Delta\rho(B \parallel ab)$, as a function of

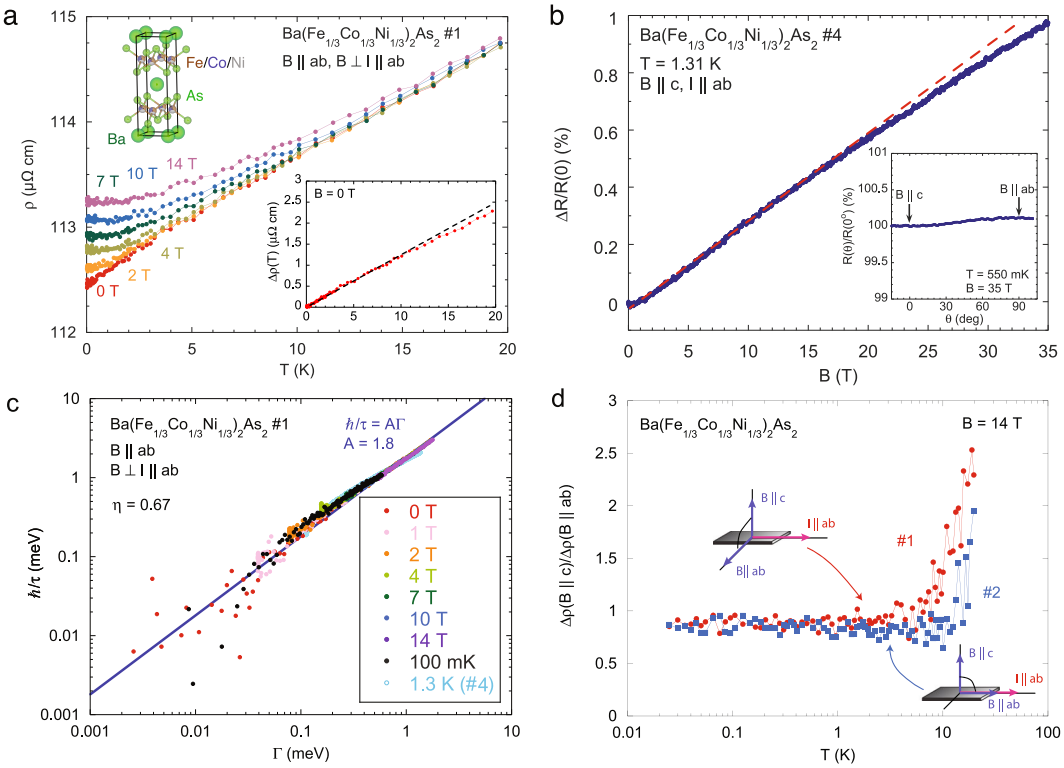

Fig. 1 Scale invariance in the resistivity of $Ba(Fe_{1/3}Co_{1/3}Ni_{1/3})_2As_2$. **a** Temperture dependence of resistivity of $Ba(Fe_{1/3}Co_{1/3}Ni_{1/3})_2As_2$ in the configuration of $B \parallel ab$, $B \perp I \parallel ab$. Upper inset: crystal structure for $Ba(Fe_{1/3}Co_{1/3}Ni_{1/3})_2As_2$ (ref. [46]). Lower inset: $\Delta\rho(T) = \rho(T) - \rho(0))$ as a function of T at $B = 0$ T for $Ba(Fe_{1/3}Co_{1/3}Ni_{1/3})_2As_2$. A dashed line is a guide to the eye to highlight quasi-linear-in-T dependence of resistivity. **b** Magnetic field dependence of $\Delta R(B)/R(0) \equiv (R(1.31\,\mathrm{K}, B) - R(1.31\,\mathrm{K}, 0))/R(1.31\,\mathrm{K}, 0)$ at $T = 1.31$ K. A red dashed line is a guide to the eye to highlight sublinear-in-B behavior of magnetoresistance. Inset: angular dependence of magnetoresistance at $T = 550$ mK and $B(\parallel c \perp I) = 35$ T. **c** Inelastic scattering rate $\hbar/\tau$ as a function of $\Gamma = \sqrt{(k_B T)^2 + (\eta\mu_B B)^2}$, with $\eta = 0.67$, suggestive of a universal scale invariance in the scattering mechanism in $Ba(Fe_{1/3}Co_{1/3}Ni_{1/3})_2As_2$. A blue sold line is a linear fit to data using $\hbar/\tau = A\Gamma$ with $A = 1.8$. **d** Temperature dependence of anisotropy of magnetoresistance between $\Delta\rho(B \parallel c)$ and $\Delta\rho(B \parallel ab \perp I$; sample #1) and between $\Delta\rho(B \parallel c)$ and $\Delta\rho(B \parallel ab \parallel I$; sample #2) at $B = 14$ T, showing lack of anisotropy in the scattering rate.

temperature in Fig. 1d. The anisotropy between transverse MR in the out-of-plane field ($B \parallel c$, $I \parallel ab$) and transverse MR in the in-plane field ($B \parallel ab$, $B \perp I \parallel ab$) decreases down to unity with decreasing temperatures, suggesting the spatial dimension of the system is three. The isotropy in MR remains even at 35 T, as shown in the angular dependence of MR (Fig. 1 inset). Due to the three dimensionality, we observe similar $\Gamma(T, B)$ scaling in the resistivity regardless of applied field orientations (Supplementary Note 3). Moreover, the observed positive MR appears not to be driven by the orbital effect due to the Lorentz force, but rather associated with Zeeman energy-tuned scattering, evidenced by the isotropy in the MR between in-plane transverse ($B \parallel c$, $I \parallel ab$) and longitudinal ($B \parallel I \parallel ab$) configurations (Fig. 1d).

Thermodynamic properties. In addition to resistivity, magnetic susceptibility $\chi = M/B$ and electronic heat capacity C_e/T also exhibit canonical NFL behavior, i.e., diverging temperature dependence associated with QC instabilities[26]. The magnetic susceptibility varies as $\chi \propto T^{-1/3}$ at low temperatures <8 K (inset of Fig. 2a), in contrast to the T-independent Pauli paramagnetic susceptibility $\chi_P = 2g\mu_B^2 D(E_F)$ (with electron g-factor and density of states at the Fermi energy $D(E_F)$) observed in FL metals, and observed upon increasing magnetic field to 7 T (Fig. 2a). A similar crossover is also observed in the heat capacity. Obtained form the subtraction of phonon (C_{ph}) and nuclear Schottky contributions (C_{Sch}) from the total heat capacity (C_{tot}), the electronic specific heat coefficient $C_e/T = (C_{tot} - C_{ph} - C_{Sch})/T$ exhibits power law divergence, $C_e/T \sim T^{-0.25}$ (Supplementary Note 4), stronger than logarithmic in the temperature dependence down to ~150 mK (Fig. 2b). Diminished with applying field, the NFL behavior observed in zero field completely disappears at applied field of 10 T, indicative of the recovery of FL (Supplementary Note 5). We note that the obtained specific heat coefficient $\gamma = C_e/T$ at $B = 0$ T, combined with the magnetic susceptibility χ, provides large Wilson ratio $R_W = \pi^2 k_B^2 \chi / 3\mu_B^2 \gamma = 3.2$ at $T = 1.8$ K, suggestive of the presence of magnetic instabilities similar to $BaCo_2As_2$.

The observation of FL recovery with magnetic field corroborates the presence of a new energy scale $k_B T^*$, distinctive of crossover between the QC ($k_B T \gg g\mu_B B$) and FL ($k_B T \ll g\mu_B B$) regimes. Intriguingly, this new energy scale allows a single scaling function of T/B in the magnetization, written by,

$$-\frac{dM}{dT} = B^{-\frac{1}{3}} f_M\left(\frac{T}{B}\right), \quad (1)$$

as shown in Fig. 2c. This scaling relation indeed reveals the underlying free energy given by a universal function of T/B,

$$F(T, B) = B^{(d+z)/y_b} f_F\left(\frac{T}{B^{z/y_b}}\right), \quad (2)$$

where d is the spatial dimensionality, z is the dynamic exponent, and y_b is the scaling exponent related to the tuning parameter B (refs. [27–30]). Here, $f_F(x)$ is a universal function of x. Hence, the magnetization can be derived from the derivative of the free

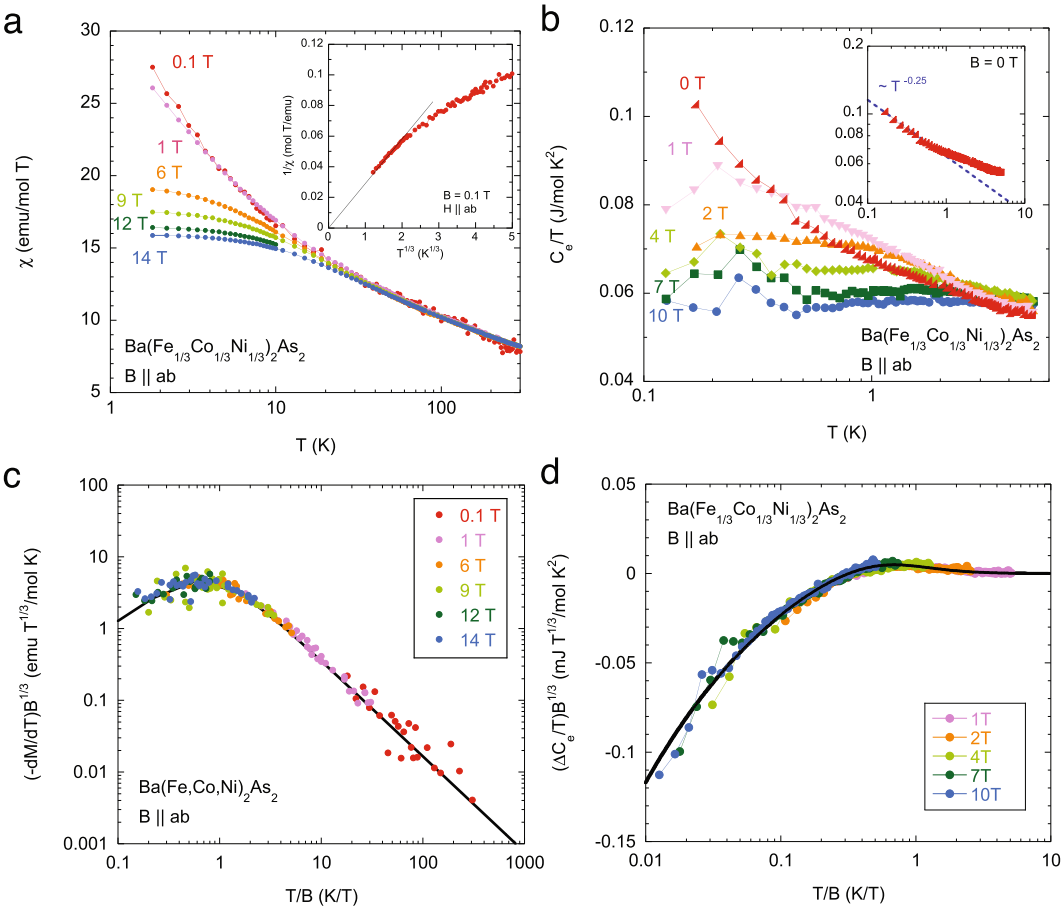

Fig. 2 Non-Fermi liquid to Fermi liquid crossover and scale invariance in thermodynamic quantities. a Temperature dependence of magnetic susceptibility for $Ba(Fe_{1/3}Co_{1/3}Ni_{1/3})_2As_2$ ($B \parallel ab$). Inset: $1/\chi$ as a function of $T^{1/3}$ at low temperatures. **b** Electronic specific heat $C_e/T = (C_{tot} - C_{sch} - C_{ph})/T$ for $Ba(Fe_{1/3}Co_{1/3}Ni_{1/3})_2As_2$ under several fields parallel to *ab*-plane. Inset: log–log plot for C_e/T vs T for $B = 0$ T. The dashed line emphasizes the $T^{-0.25}$-power law behavior observed <1 K. **c** Temperature-magnetic field scale invariance in magnetization and **d** specific heat. The measured magnetization and specific heat collapse onto universal scaling curves in the forms of $-dM/dT = B^{-1/3}f_M(T/B)$ and $\Delta C_e/T = B^{-1/3}g_C(T/B)$, respectively, indicating the presence of the underlying free energy given by a universal function of T/B and the existence of the quantum critical point located at $T = 0$ and $B = 0$. Black lines represent scaling functions $f_M(T/B)$ for magnetization and $g_C(T/B)$ for specific heat derived from the underlying free energy, described in the main text.

energy,

$$-\frac{dM}{dT} = -\frac{d}{dT}\left(\frac{dF}{dB}\right) = B^{d/y_b - 1} f_M\left(\frac{T}{B^{z/y_b}}\right). \quad (3)$$

Directly comparing this with the observed QC scaling relation in Fig. 2c, we can extract the critical exponents in the free energy, namely, $z/y_b = 1$ and $d/y_b - 1 = -1/3$, yielding $z = y_b$ and $d/z = 2/3$. These values of the critical exponents describe the specific heat by using the same free energy,

$$\frac{C_e(B,T)}{T} = -\frac{\partial^2 F}{\partial T^2} = B^{\frac{d-z}{y_b}} f_C\left(\frac{T}{B^{z/y_b}}\right). \quad (4)$$

Rewriting the free energy, $F(T,B) = B^{\frac{d+z}{y_b}} f(T/B^{z/y_b}) = T^{\frac{d+z}{z}} \tilde{f}(B/T^{y_b/z})$, we find

$$\frac{\Delta C_e(T,B)}{T} = \frac{C_e(T,B)}{T} - \frac{C_e(T,0)}{T} = B^{-\frac{1}{3}} g_C\left(\frac{T}{B}\right), \quad (5)$$

where $g_C(x)$ is field-dependent part of $f_C(x)$ (Supplementary Notes 6 and 7). As demonstrated in Fig. 2d, this expression illustrates scale invariance in the specific heat that persists over nearly three orders of magnitude in the scaling variable T/B.

Hall resistivity and electronic structure. The T/B scaling in thermodynamics clearly discloses the presence of the QCP located exactly at zero field and absolute zero, similar to the layered QC metals $YbAlB_4$ (ref. [31]) and YFe_2Al_{10} (ref. [32]). More notably, the multiband nature in iron pnictides affixes the uniqueness of quantum criticality for $Ba(Fe_{1/3}Co_{1/3}Ni_{1/3})_2As_2$. Dominated by electron-like carriers, the Hall resistivity ρ_{yx} is negative and perfectly linear in field at high temperatures ($T = 20$ K), as shown in Fig. 3a. Upon cooling, ρ_{yx} develops a nonlinearity with negative curvature. More prominent <1 K, the nonlinear Hall resistivity switches its sign at low fields <2 T. The sign change is more readily observed in the temperature dependence of Hall coefficient R_H defined by ρ_{yx}/B at low-T and low-H region (Fig. 3b), implying that hole-like carriers dominate the transport in the vicinity of the QCP. The radial shape of the dominant carrier crossover in the field-temperature phase diagram confirms the absence of an intrinsic energy scale in R_H (Fig. 3c), or in other words, the presence of scale invariance in the Hall effect tuned by temperature and magnetic field. Similar to the resistivity, R_H obeys $\Gamma(T, B)$ scaling (Fig. 3d), consolidating the existence of scale invariance near the QCP in this system beyond any doubt.

Angle-resolved photoemission measurements identify a unique electronic structure and confirm the anomalous scattering rate

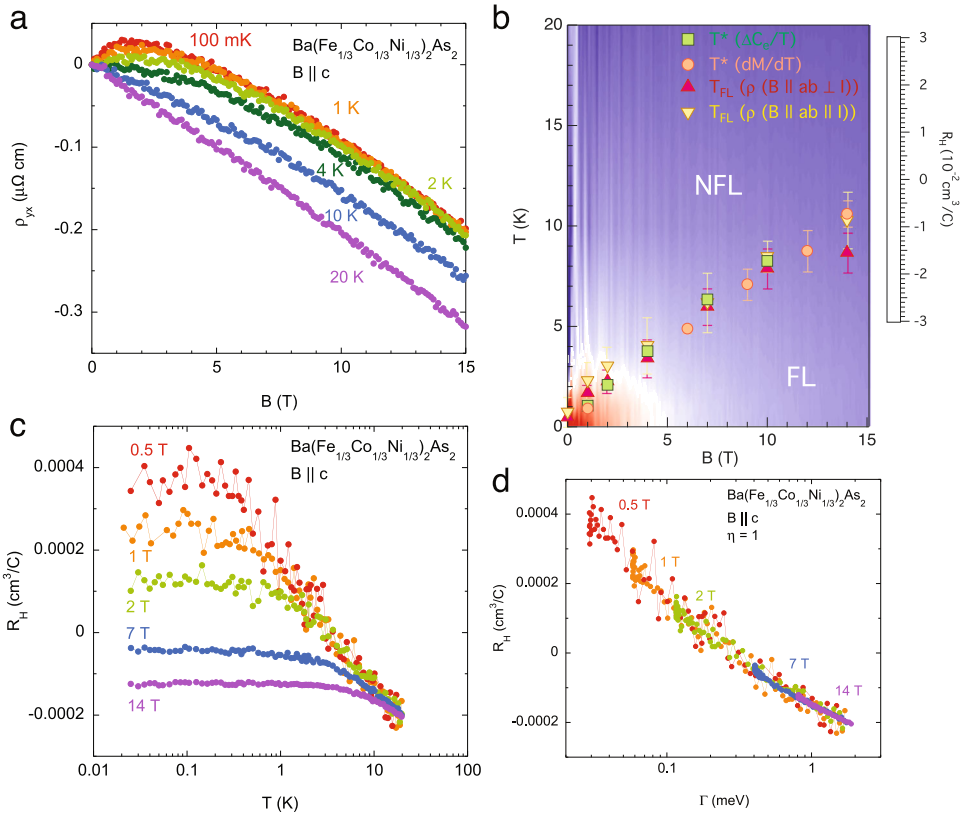

Fig. 3 Sign change due to dominant hole-like carriers near the quantum critical point and scale invariance in Hall effect. a Hall resistivity ρ_{yx} as a function of B. At high temperatures, ρ_{yx} is negative and linear in field. Upon cooling temperatures, ρ_{yx} becomes nonlinear and its sign switches to positive at low fields <2 T. **b** Temperature dependence of Hall coefficient R_H defined by ρ_{yx}/B. **c** $T-B$ phase diagram with color plot of R_H. Crossover temperatures T^* obtained from the quantum scaling in dM/dT and $\Delta C_e/T$ and T_{FL} from the T^2-fit are also plotted in the phase diagram. The error bars of T^* represent the standard deviation, and the error bars of T_{FL} are estimated by changing the fitting range. **d** R_H as a function of $\Gamma(T,B) \equiv \sqrt{(k_B T)^2 + (\eta\mu_B B)^2}$ with $\eta = 1$. All the data collapse onto one universal curve, suggesting unusual scaling between temperature and applied field similar to that found in the longitudinal resistivity.

correlated with Planckian dissipation. Unlike heavily electron-doped $BaCo_2As_2$, the electronic structure for $Ba(Fe_{1/3}Co_{1/3}Ni_{1/3})_2As_2$ consists of a large hole-like pocket and a cross-shaped electron-like Fermi surface around the Γ point, together with oval and elongated electron pockets around the M points, exhibited by the Fermi surface map (Fig. 4a), the band dispersion along $k_x = 0$ direction (Fig. 4b) at 30 K, and a schematic illustration (Fig. 4a, inset). The elongated electron pockets are very shallow, and the chemical potential is located close to the bottom of the shallow bands. Dominating transport at low temperatures and fields, the large hole-like pocket is identified as the one responsible for QC behavior. Amazingly, the scattering rate (obtained from the dispersion of the hole-like bands at 1 K) varies linearly with the kinetic energy up to 100 meV, consistent with Planckian dissipation as observed in the resistivity (Fig. 4c, d).

Discussion

While our primary observations of the scale invariance in the thermodynamics are consistent with quantum criticality overall, they indicate a highly unusual critical behavior in $Ba(Fe_{1/3}Co_{1/3}Ni_{1/3})_2As_2$. While sharing an enhancement of the Wilson ratio with $BaCo_2As_2$ indicative of a FM instability, the critical behavior in $Ba(Fe_{1/3}Co_{1/3}Ni_{1/3})_2As_2$ is not described by any known theoretical predictions. Assuming spacial dimensionality of three ($d = 3$) based on the observed isotropic response in MR and magnetization (Supplementary Note 3), the observed critical exponents of $d/z = 2/3$ and $z = y_b$ yield $z = y_b = 4.5$.

The extracted dynamical exponents from our measurements do not match the predictions for either mean-field Hertz–Moriya–Millis theory for $d = 3$ (which predict $z = 3$ for clean FM and $z = 4$ for dirty FM quantum criticality with $\nu = 1/2$)[27–29], or predictions for clean FM beyond mean field, which predict the appearance of a weak first-order transition, with $z = 3$ and $\nu = 1/4$ for $d = 3$ and quantum wing critical points with the same critical exponents, as the mean-field theory[33–37]. QC behavior in disordered 3d FM has been well explained by the Belitz–Kirkpatrick–Vojta theory, predicting critical exponents $\nu = 1$ and $z = 3$ for the asymptotic limit, and $\nu = 0.25$ and $z = 6$ for the preasymptotic limit[37, 38], neither of which is in agreement with our observation. Experimentally, previously measured exponents in QC materials, such as $YbNi_4(P_{1-x}As_x)_2$ (FM QCP, $\nu z \sim 5$)[39], $CeCu_{6-x}Au_x$ (AFM QCP, $d/z = 1/4$, $\nu z = 1$)[40], β-$YbAlB_4$ (mixed-valence meal, $d/z = 1/2$, $\nu z = 1$)[31], YFe_2Al_{10} (layered QC metal, $d/z = 1$, $\nu z = 0.59$)[32], and $Sr_{0.3}Ca_{0.7}RuO_3$ (disordered FM QCP, $z = 1.76$)[41] are also incompatible with the measured dynamical exponent.

The high residual resistivity observed in $Ba(Fe_{1/3}Co_{1/3}Ni_{1/3})_2As_2$ evokes the possible realization of quantum Griffiths phase, where the QC behavior is dominated by FM rare regions. The quantum Griffiths model predicts power law singularities in the magnetic susceptibility ($\chi \sim T^{\lambda-1}$), specific heat ($C/T \sim T^{\lambda-1}$), and magnetization ($M \sim B^{\lambda}$), determined by the nonuniversal Griffiths exponent λ that takes 0 at the QCP, and increases with distance from criticality[42]. In the present system, however, $\lambda = 2/3$ extracted from the magnetic susceptibility ($\chi \sim T^{-1/3}$; Fig. 1a inset) disagrees with $\lambda = 0.75$ obtained from the specific heat ($C/T \sim T^{-0.25}$; Fig. 2b inset), irreconcilable with the quantum Griffiths model. Besides, the critical exponents in $Ba(Fe_{1/3}Co_{1/3}Ni_{1/3})_2As_2$ do not agree with those obtained experimentally in other quantum Griffith systems[37]. For instance, disordered weak ferromagnet $Ni_{1-x}V_x$ show critical

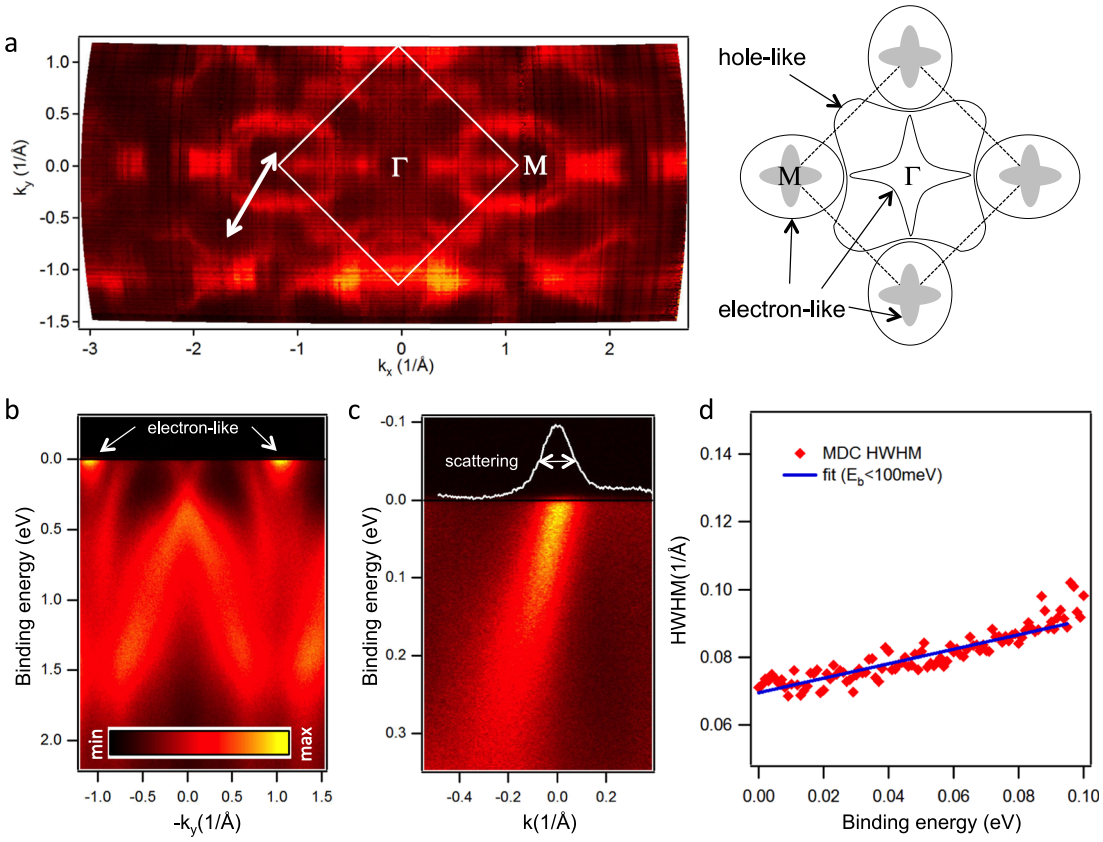

Fig. 4 Fermi surfaces and anomalous scattering rates in $Ba(Fe_{1/3}Co_{1/3}Ni_{1/3})_2As_2$. a Angle-resolved photoemission study of Fermi surface map for Ba $(Fe_{1/3}Co_{1/3}Ni_{1/3})_2As_2$, measured at 30 K. White lines denote the Brillouin zone (BZ) boundary, and white arrow corresponds to the cut shown in **c**. The inset depicts a schematic Fermi surface corresponding to the experimentally observed data, with shallow elongated electron pockets shown in gray. **b** Energy cut along the $k_x = 0$ direction, highlighting the elongated shallow electron-like pockets observed near the BZ corners. **c** Energy dispersion of hole-like pocket measured at 1 K near the BZ boundary along the cut indicated by white arrow in **a**, where sharp crossings of the Fermi level are found. The momentum axis originates at the crossing point. The white spectrum is the momentum distribution curve (MDC) at the Fermi level, with indicated width a representative measure of the scattering rate. **d** Scattering rate energy dependence obtained from the half width at half maximum (HWHM) of energy dispersion in panel **c**, with linear fit up to 100 meV.

behavior dominated by quantum Griffiths singularities, $\chi \sim T^{\lambda-1}$ and $M \sim B^{\lambda}$, over a wide range of vanadium concentration[43, 44]. On the other hand, in $Ba(Fe_{1/3}Co_{1/3}Ni_{1/3})_2As_2$, $\lambda = 2/3$ derived from the magnetic susceptibility contradicts λ obtained from magnetization $M \sim B^{0.75}$ (Supplementary Fig. 5), in conflict with the quantum Griffiths phase.

Highly unusual dynamical critical behavior in this material cannot be simply explained by existing FM QCP theories, but instead, it can be attributed to substitutional alloying by counter-doping. Indeed, the anomalous behavior observed in $Ba(Fe_{1/3}Co_{1/3}Ni_{1/3})_2As_2$ is more prominent than that observed in both of the end members of the $3d^7$ configuration line, namely, $BaCo_2As_2$ and $Ba(Fe,Ni)_2As_2$ (Supplementary Notes 8 and 9), signifying that the specific 1/3 equal ratios of Fe:Co:Ni in $BaCo_2As_2$ are indeed important to stabilizing a unique QC ground state. In fact, as shown in Fig. 5, the observed NFL scattering behavior in $Ba(Fe_{1/3}Co_{1/3}Ni_{1/3})_2As_2$ is completely robust against pressure and even replacement of Ba for Sr (i.e., in $Sr(Fe_{1/3}Co_{1/3}Ni_{1/3})_2As_2$), implying either an electronic structure modification beyond d electron tuning, or a significant role for transition metal site dilution. In fact, while generally obscuring the critical behavior, high randomness due to substitution indeed plays an important role in some QC materials, such as medium entropy alloys[38, 45], in which similar NFL behavior has been realized[38, 45]. Together with the pressure insensitivity of the T-linear scattering in $Ba(Fe_{1/3}Co_{1/3}Ni_{1/3})_2As_2$, our experimental observations of scale invariance in this system indicates that substitutional alloying is a key ingredient to tune the quantum criticality that may provide the key to understanding the lack of superconductivity driven by QC fluctuations.

Methods

Sample preparation. The single crystals of $Ba(Fe_{1/3}Co_{1/3}Ni_{1/3})_2As_2$ were grown by TMAs (TM = Fe, Co, and Ni) self-flux method with the molar ratios of 3:4:4:4 = Ba:FeAs:CoAs:NiAs. Resulting crystals were cleaved out of the flux. The typical crystal size is $5 \times 5 \times 0.1$ mm^3.

Magnetotransport measurements. Magnetotransport measurements up to 15 T were conducted in a ^3He–^4He dilution refrigerator, and high magnetic field transport measurements up to 35 T were performed at the National High Magnetic Field Laboratory in Tallahassee.

Heat capacity measurements. Heat capacity was measured using the thermal relaxation method in a ^3He–^4He dilution refrigerator. A RuO_2 thermometer on the calorimeter was calibrated in magnetic fields up to 15 T.

Magnetic susceptibility measurements. Magnetic susceptibility was measured using the vibrating sample magnetometer option in a 14 T Quantum Design DynaCool Physical Properties Measurement System and a 7 T SQUID Magnetic Properties Measurement System.

Pressure measurements. A nonmagnetic piston–cylinder pressure cell was used for transport measurements under pressure up to 1.99 GPa, using a 1:1 ratio of n-pentane to 1-methyl-3-butanol as the pressure medium, and superconducting temperature of lead as pressure gauge at base temperature. All transport measurements were performed on the same $Ba(Fe_{1/3}Co_{1/3}Ni_{1/3})_2As_2$ crystal with 200

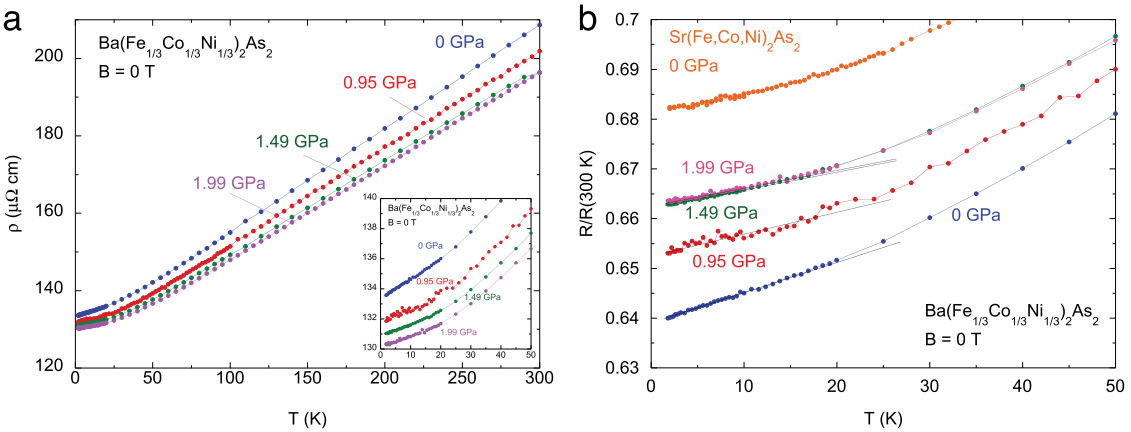

Fig. 5 Robust non-Fermi liquid behavior against pressure. a Overall temperature dependence of resistivity for $Ba(Fe_{1/3}Co_{1/3}Ni_{1/3})_2As_2$ under applied pressure. The linear-*T* resistivity <20 K is robust against applying pressure up to 1.99 GPa as shown in the inset. **b** Normalized resistance *R*/*R*(300 K) vs *T* under pressure. On applying pressure, *R*/*R*(300 K) for $Ba(Fe_{1/3}Co_{1/3}Ni_{1/3})_2As_2$ increases, approaching that for $Sr(Fe_{1/3}Co_{1/3}Ni_{1/3})_2As_2$ with smaller lattice constants than $Ba(Fe_{1/3}Co_{1/3}Ni_{1/3})_2As_2$ (Supplementary Notes 10 and 11, and Supplementary Table 1), indicative of robustness of linear-*T* behavior in the resistivity against pressure.

μm thickness, using four point contacts made with silver epoxy. The pressure and temperature dependence of the resistivity were measured during warming process in a Quantum Design Physical Properties Measurement System. Mention of commercial equipment does not imply endorsement by NIST.

Angle-resolved photoemission spectroscopy. Angle-resolved photoemission spectroscopy for $Ba(Fe_{1/3}Co_{1/3}Ni_{1/3})_2As_2$ was performed using the 1^3-ARPES end station of the UE112-PGM2b beam-line at BESSY II (Helmholtz Zentrum Berlin) synchrotron radiation center.

Data availability

All data presented in this manuscript are available from the corresponding author upon reasonable request.

Received: 25 June 2020; Accepted: 11 September 2020;
Published online: 15 October 2020

References

1. Paglione, J. & Greene, R. L. High-temperature superconductivity in iron-based materials. *Nat. Phys.* **6**, 645–658 (2010).
2. Shibauchi, T., Carrington, A. & Matsuda, Y. A quantum critical point lying beneath the superconducting dome in iron pnictides. *Annu. Rev. Condens. Matter Phys.* **5**, 113–135 (2014).
3. Mazin, I. I., Singh, D. J., Johannes, M. D. & Du, M. H. Unconventional superconductivity with a sign reversal in the order parameter of $LaFeAsO_{1-x}F_x$. *Phys. Rev. Lett.* **101**, 057003 (2008).
4. Kuroki, K., Usui, H., Onari, S., Arita, R. & Aoki, H. Pnictogen height as a possible switch between high-T_c nodeless and low-T_c nodal pairings in the iron-based superconductors. *Phys. Rev. B* **79**, 224511 (2009).
5. Hayes, I. M. et al. Scaling between magnetic field and temperature in the high-temperature superconductor $BaFe_2(As_{1-x}P_x)_2$. *Nat. Phys.* **12**, 916–919 (2016).
6. Giraldo-Gallo, P. et al. Scale-invariant magnetoresistance in a cuprate superconductor. *Science* **361**, 479–481 (2018).
7. Legros, A. et al. Universal T-linear resistivity and planckian dissipation in overdoped cuprates. *Nat. Phys.* **15**, 142–147 (2019).
8. Guo, H., Gu, Y. & Sachdev, S. Linear in temperature resistivity in the limit of zero temperature from the time reparameterization soft mode. *Ann. Phys.* **418**, 168202 (2020).
9. Chu, J.-H. et al. In-plane resistivity anisotropy in an underdoped iron arsenide superconductor. *Science* **329**, 824–826 (2010).
10. Yi, M. et al. Symmetry-breaking orbital anisotropy observed for detwinned Ba $(Fe_{1-x}Co_x)_2As_2$ above the spin density wave transition. *Proc. Natl Acad. Sci. USA* **108**, 6878–6883 (2011).
11. Nakajima, M. et al. Unprecedented anisotropic metallic state in undoped iron arsenide $BaFe_2As_2$ revealed by optical spectroscopy. *Proc. Natl Acad. Sci. USA* **108**, 12238–12242 (2011).
12. Chu, J.-H., Kuo, H.-H., Analytis, J. G. & Fisher, I. R. Divergent nematic susceptibility in an iron arsenide superconductor. *Science* **337**, 710–712 (2012).
13. Yanagi, H. et al. Itinerant ferromagnetism in the layered crystals LaCoOX (X=P,As). *Phys. Rev. B* **77**, 224431 (2008).
14. Anand, V. K. et al. Crystallography and physical properties of $BaCo_2As_2$, $Ba_{0.94}K_{0.06}Co_2As_2$, and $Ba_{0.78}K_{0.22}Co_2As_2$. *Phys. Rev. B* **90**, 064517 (2014).
15. Wiecki, P. et al. Competing magnetic fluctuations in iron pnictide superconductors: role of ferromagnetic spin correlations revealed by NMR. *Phys. Rev. Lett.* **115**, 137001 (2015).
16. Wiecki, P., Ogloblichev, V., Pandey, A., Johnston, D. C. & Furukawa, Y. Coexistence of antiferromagnetic and ferromagnetic spin correlations in $SrCo_2As_2$ revealed by ^{59}Co and ^{75}As NMR. *Phys. Rev. B* **91**, 220406 (2015).
17. Sefat, A. S. et al. Renormalized behavior and proximity of $BaCo_2As_2$ to a magnetic quantum critical point. *Phys. Rev. B* **79**, 024512 (2009).
18. Sefat, A. S. et al. Structure and anisotropic properties of $BaFe_2-xNi_xAs_2$ (x = 0, 1, and 2) single crystals. *Phys. Rev. B* **79**, 094508 (2009).
19. Eckberg, C. et al. Evolution of structure and superconductivity in $Ba(Ni_{1-x}Co_x)_2As_2$. *Phys. Rev. B* **97**, 224505 (2018).
20. Ni, N. et al. Phase diagrams of $Ba(Fe_{1-x}M_x)_2As_2$ single crystals (M=Rh and Pd). *Phys. Rev. B* **80**, 024511 (2009).
21. Canfield, P. C., Bud'ko, S. L., Ni, N., Yan, J. Q. & Kracher, A. Decoupling of the superconducting and magnetic/structural phase transitions in electron-doped $BaFe_2As_2$. *Phys. Rev. B* **80**, 060501 (2009).
22. Liu, C. et al. Evidence for a lifshitz transition in electron-doped iron arsenic superconductors at the onset of superconductivity. *Nat. Phys.* **6**, 419–423 (2010).
23. Neupane, M. et al. Electron-hole asymmetry in the superconductivity of doped $BaFe_2As_2$ seen via the rigid chemical-potential shift in photoemission. *Phys. Rev. B* **83**, 094522 (2011).
24. Ciuchi, S., Di Sante, D., Dobrosavljević, V. & Fratini, S. The origin of mooij correlations in disordered metals. *npj Quantum Mater.* **3**, 44 (2018).
25. Lee, P. A. & Ramakrishnan, T. V. Disordered electronic systems. *Rev. Mod. Phys.* **57**, 287–337 (1985).
26. Stewart, G. Non-fermi-liquid behavior in d- and f-electron metals. *Rev. Mod. Phys.* **73**, 797 (2001).
27. Hertz, J. A. Quantum critical phenomena. *Phys. Rev. B* **14**, 1165 (1976).
28. Moriya, T. *Spin Fluctuations in Itinerant Electron Magnetism* (Springer, Berlin, Heidelberg, Germany, 1985).
29. Millis, A. J. Effect of a nonzero temperature on quantum critical points in itinerant fermion systems. *Phys. Rev. B* **48**, 7183–7196 (1993).
30. Sachdev, S. *Quantum Phase Transitions* (Cambridge University Press, Cambridge, UK, 1999).
31. Matsumoto, Y. et al. Quantum criticality without tuning in the mixed valence compound β-$YbAlB_4$. *Science* **331**, 316–319 (2011).
32. Wu, L. S., Kim, M. S., Park, K., Tsvelik, A. M. & Aronson, M. C. Quantum critical fluctuations in layered YFe_2Al_{10}. *Proc. Natl Acad. Sci. USA* **111**, 14088–14093 (2014).
33. Belitz, D., Kirkpatrick, T. R. & Vojta, T. Nonanalytic behavior of the spin susceptibility in clean fermi systems. *Phys. Rev. B* **55**, 9452–9462 (1997).

34. Rech, J., Pépin, C. & Chubukov, A. V. Quantum critical behavior in itinerant electron systems: Eliashberg theory and instability of a ferromagnetic quantum critical point. *Phys. Rev. B* **74**, 195126 (2006).
35. Conduit, G. J., Green, A. G. & Simons, B. D. Inhomogeneous phase formation on the border of itinerant ferromagnetism. *Phys. Rev. Lett.* **103**, 207201 (2009).
36. Kirkpatrick, T. R. & Belitz, D. Exponent relations at quantum phase transitions with applications to metallic quantum ferromagnets. *Phys. Rev. B* **91**, 214407 (2015).
37. Brando, M., Belitz, D., Grosche, F. M. & Kirkpatrick, T. R. Metallic quantum ferromagnets. *Rev. Mod. Phys.* **88**, 025006 (2016).
38. Sales, B. C. et al. Quantum critical behavior in the asymptotic limit of high disorder in the medium entropy alloy $NiCoCr_{0.8}$. *npj Quantum Mater.* **2**, 33 (2017).
39. Steppke, A. et al. Ferromagnetic quantum critical point in the heavy-fermion metal $YbNi_4(P_{1-x}As_x)_2$. *Science* **339**, 933–936 (2013).
40. Schroeder, A. et al. Onset of antiferromagnetism in heavy-fermion metals. *Nature* **407**, 351 (2000).
41. Huang, C. L. et al. Anomalous quantum criticality in an itinerant ferromagnet. *Nat. Commun.* **6**, 8188 (2015).
42. Vojta, T. Quantum griffiths effects and smeared phase transitions in metals: theory and experiment. *J. Low. Temp. Phys.* **161**, 299–323 (2010).
43. Ubaid-Kassis, S., Vojta, T. & Schroeder, A. Quantum griffiths phase in the weak itinerant ferromagnetic alloy $Ni_{1-x}\mathbf{V}_x$. *Phys. Rev. Lett.* **104**, 066402 (2010).
44. Wang, R. et al. Quantum griffiths phase inside the ferromagnetic phase of $Ni_{1-x}V_x$. *Phys. Rev. Lett.* **118**, 267202 (2017).
45. Sales, B. C. et al. Quantum critical behavior in a concentrated ternary solid solution. *Sci. Rep.* **6**, 26179 (2016).
46. Momma, K. & Izumi, F. *VESTA3* for three-dimensional visualization of crystal, volumetric and morphology data. *J. Appl. Crystallogr.* **44**, 1272–1276 (2011).

Acknowledgements

Experimental research was supported by the National Science Foundation Division of Materials Research Award No. DMR-1610349, and materials development supported by the Gordon and Betty Moore Foundation's EPiQS Initiative through grant no. GBMF9071. A portion of this work was performed at the National High Magnetic Field Laboratory, which is supported by National Science Foundation Cooperative Agreement No. DMR-1644779 and the State of Florida. Pressure measurements were supported by NIST.

Author contributions

Y.N., T.M., K.K., A.H., and R.W. performed the low-temperature transport and heat capacity measurements, and analyzed the data. C.E. and S.R.S. grew and characterized single crystals. I.L. and N.B. conducted the pressure measurements, and D.C., Y.S.E., and D.G. performed transport measurements at high magnetic fields. Z.L. and S.V.B. measured the angle-resolved photoemission spectroscopy, and L.W. performed the theoretical support. P.Y.Z. performed the single-crystal x-ray diffraction. Y.N. and J.P. conceived and designed the experiments, and all authors contributed to the editing of the manuscript.

Competing interests

The authors declare no competing interests.

Additional information

Supplementary information is available for this paper at https://doi.org/10.1038/s42005-020-00448-5.

Correspondence and requests for materials should be addressed to Y.N. or J.P.

Supplementary Information

SUPPLEMENTARY FIGURES

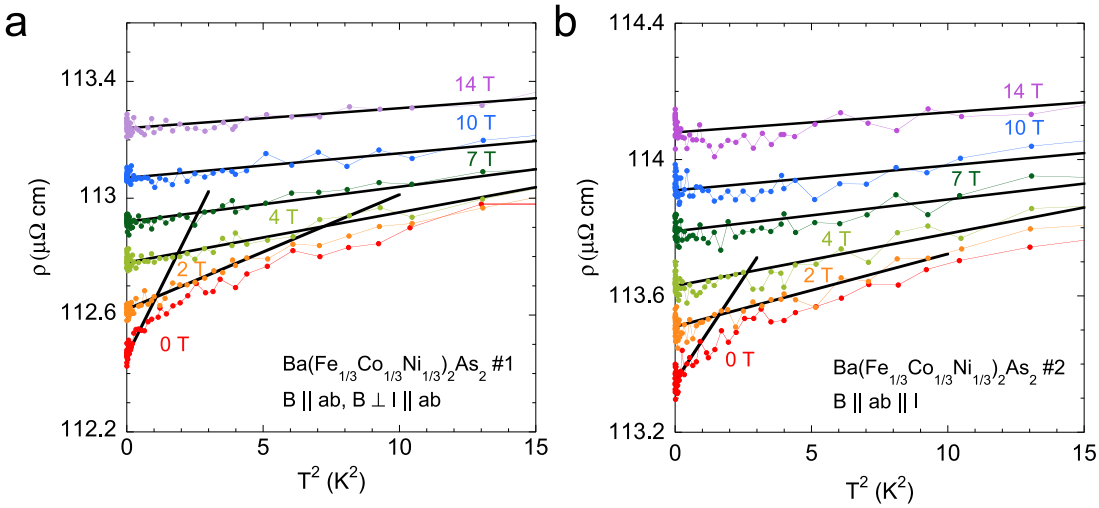

Supplementary Figure 1: **Non-Fermi liquid to Fermi liquid crossover in the resistivity for $BaCo_2As_2$.** **a**, Resistivity as a function of T^2 for sample #1 in the configuration of $B \parallel ab, B \perp I \parallel ab$ and **b**, for sample #1 in the configuration of $B \parallel ab \parallel I$. Solid lines are linear fits to the data using $\rho = \rho_0 + AT^2$.

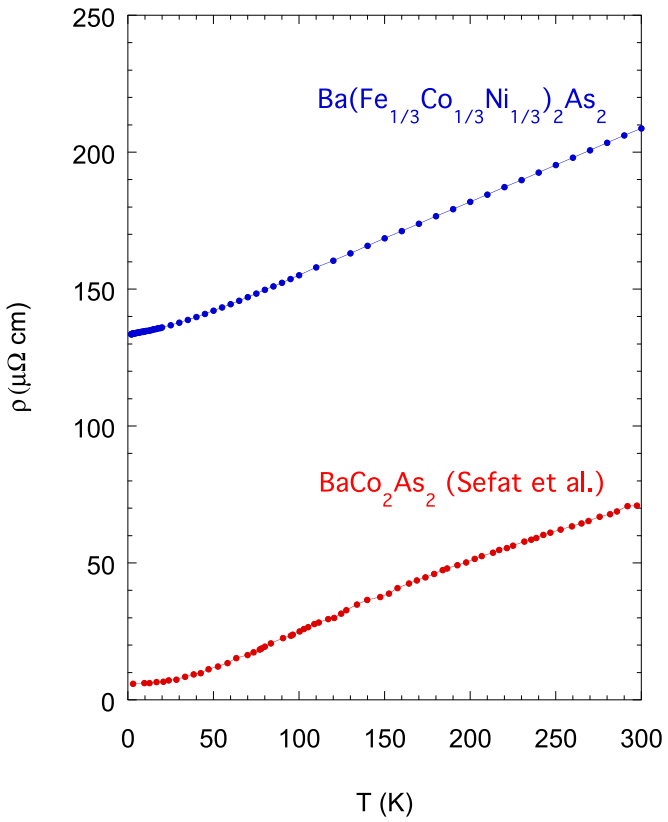

Supplementary Figure 2: **Absence of Mooij correlations.** Temperature dependence of resistivity for clean $BaCo_2As_2$ (taken from [1]) and highly disordered $Ba(Fe_{1/3}Co_{1/3}Ni_{1/3})_2As_2$. Introduction of disorder causes no change of the slop of resistivity at high temperatures, inconsistent with the Mooij correlations.

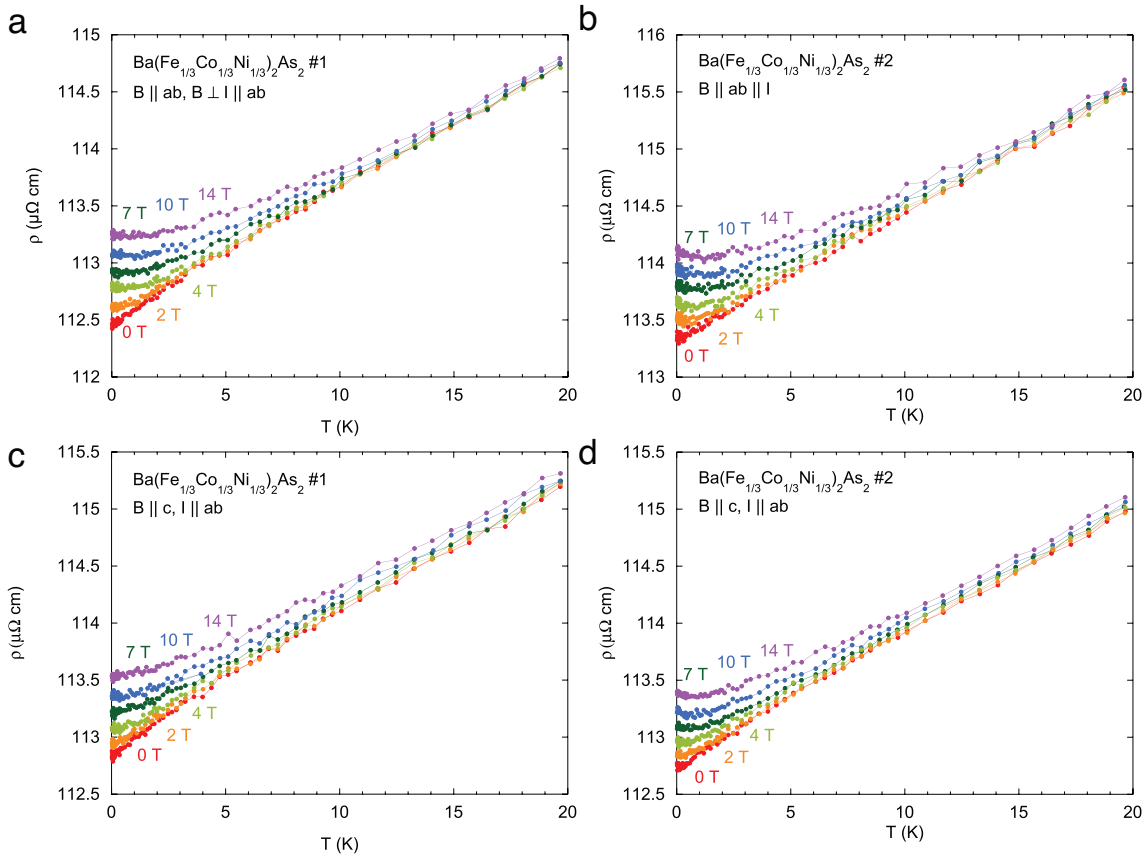

Supplementary Figure 3: **Isotropic magnetoresistance for $\mathbf{Ba(Fe_{1/3}Co_{1/3}Ni_{1/3})_2As_2}$.** Resistivity as a function of T for **a**, sample #1 with $B \parallel ab$ and $B \perp I \parallel ab$, **b**, sample #2 with $B \parallel I \parallel ab$, **c**, sample #1 with $B \parallel c$ and $BI \parallel ab$, and **d**, sample #2 with $B \parallel c$ and $BI \parallel ab$.

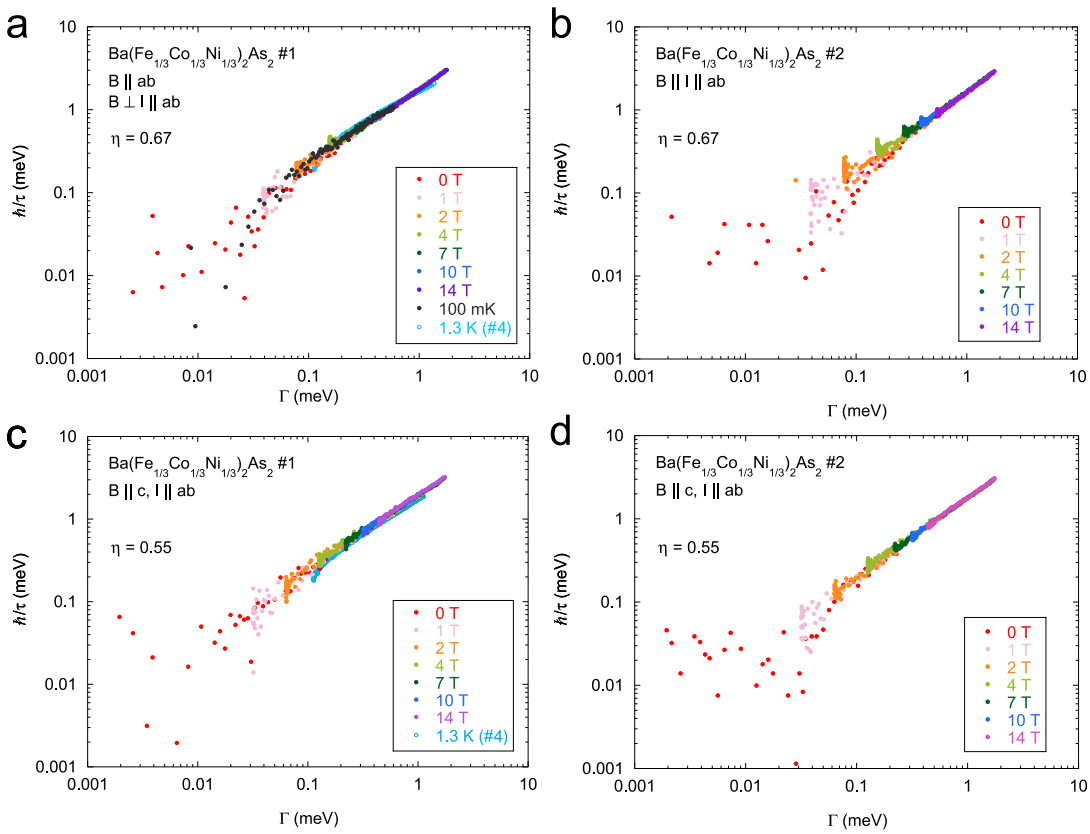

Supplementary Figure 4: Anisotropy of Γ(T,B) scaling for $Ba(Fe_{1/3}Co_{1/3}Ni_{1/3})_2As_2$ with different field orientations. Resistivity as a function of $\Gamma \equiv \sqrt{(k_B T)^2 + (\eta \mu_B B)^2}$ for **a**, sample #1 with $B \parallel ab$ and $B \perp I \parallel ab$ together with sample #4 (scaled), **b**, sample #2 with $B \parallel I \parallel ab$, **c**, sample #1 together with sample #4 (scaled) and **d**, #2 with $B \parallel c$ and $I \parallel ab$.

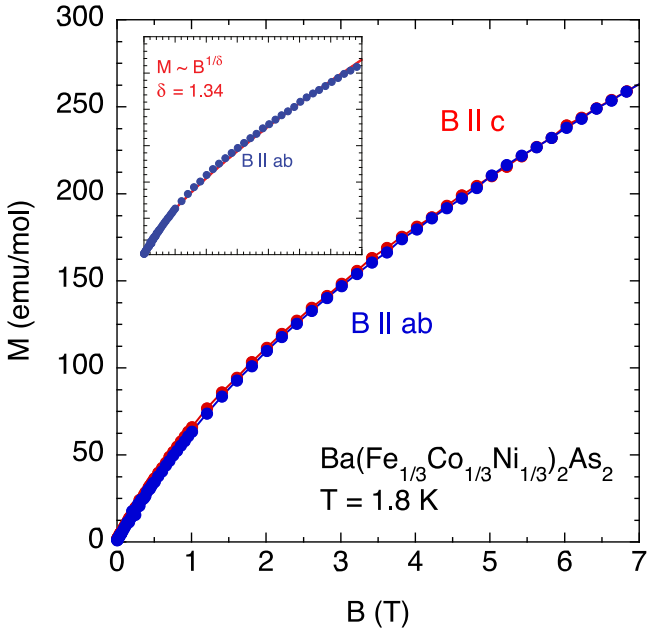

Supplementary Figure 5: **Isotropic magnetization for Ba(Fe,Co,Ni)$_2$As$_2$.** Field dependence of magnetization along $B \parallel ab$ and $B \parallel c$ at $T = 1.8$ K. Despite of the layered structure, anisotropy of magnetization is negligible, suggesting the system is three dimensional. Inset: magnetization versus B ($\parallel ab$) at 1.8 K. A red line is a fit to the data using $M \sim B^{\frac{1}{\delta}}$ with $\delta = 1.34$.

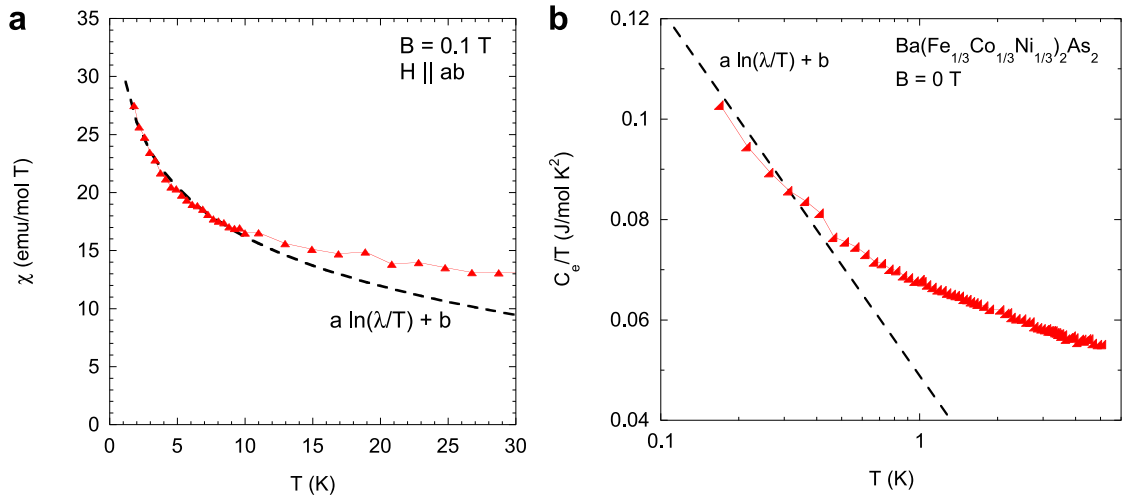

Supplementary Figure 6: **Comparison with the marginal Fermi liquid model. a,** Temperature dependence of electronic specific heat C_e/T for $Ba(Fe_{1/3}Co_{1/3}Ni_{1/3})_2As_2$ at 0 T. A dashed line is a fit to data using the marginal Fermi liquid model $a\ln(\lambda/T)+b$. **b,** temperature dependence of magnetic susceptibility χ for $Ba(Fe_{1/3}Co_{1/3}Ni_{1/3})_2As_2$ at 0.1 T. A dashed line is a fit to data using the marginal Fermi liquid model $a\ln(\lambda/T)+b$.

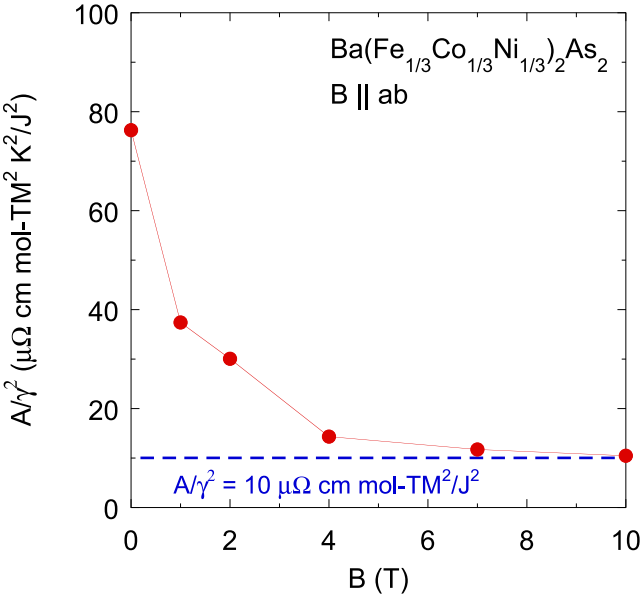

Supplementary Figure 7: **Kadowaki-Woods relation.** Field dependence of Kadowaki-Woods ratio A/γ^2 for $Ba(Fe_{1/3}Co_{1/3}Ni_{1/3})_2As_2$. A/γ^2 decreases with B, approaching $a_{KW=}$ 10 $\mu\Omega$ cm mol^2 K^2 J^{-2} at 10 T, where Fermi liquid behavior is observed in the temperature dependence of resistivity ($\rho \sim T^2$) and specific heat ($\gamma \sim$ const.) at low temperatures.

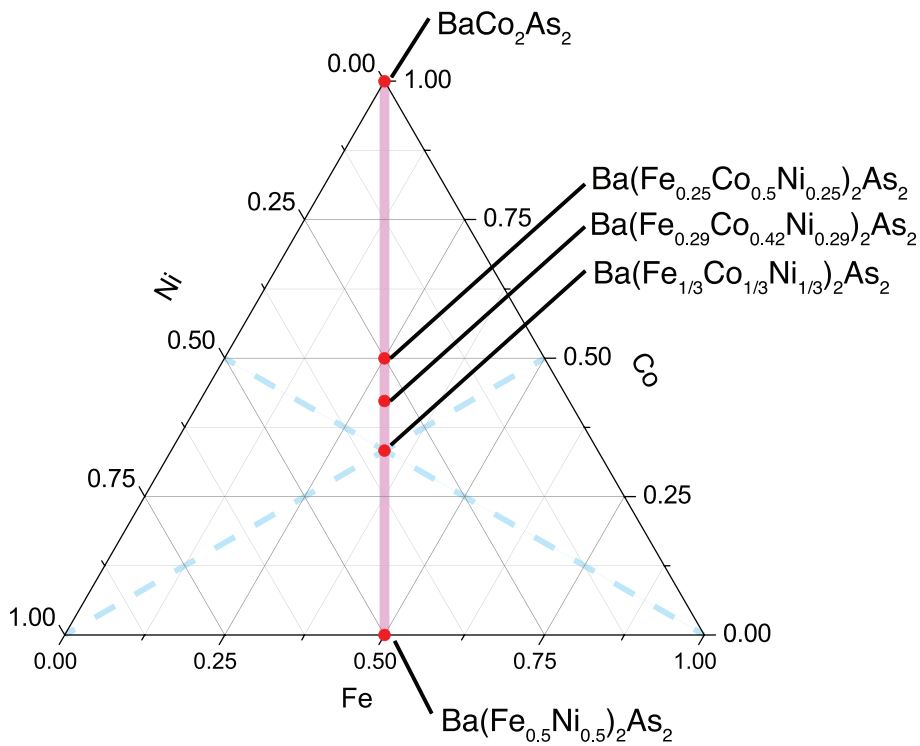

Supplementary Figure 8: **Ternary phase diagram**. A ternary phase diagram for $Ba(Fe,Co,Ni)_2As_2$. The red circles indicating the locations of $BaCo_2As_2$, $Ba(Fe_{0.25}Co_{0.5}Ni_{0.25})_2As_2$, $Ba(Fe_{0.29}Co_{0.42}Ni_{0.29})_2As_2$, $Ba(Fe_{1/3}Co_{1/3}Ni_{1/3})_2As_2$, and $Ba(Fe_{0.5}Ni_{0.5})_2As_2$, determined by energy dispersion spectroscopy.

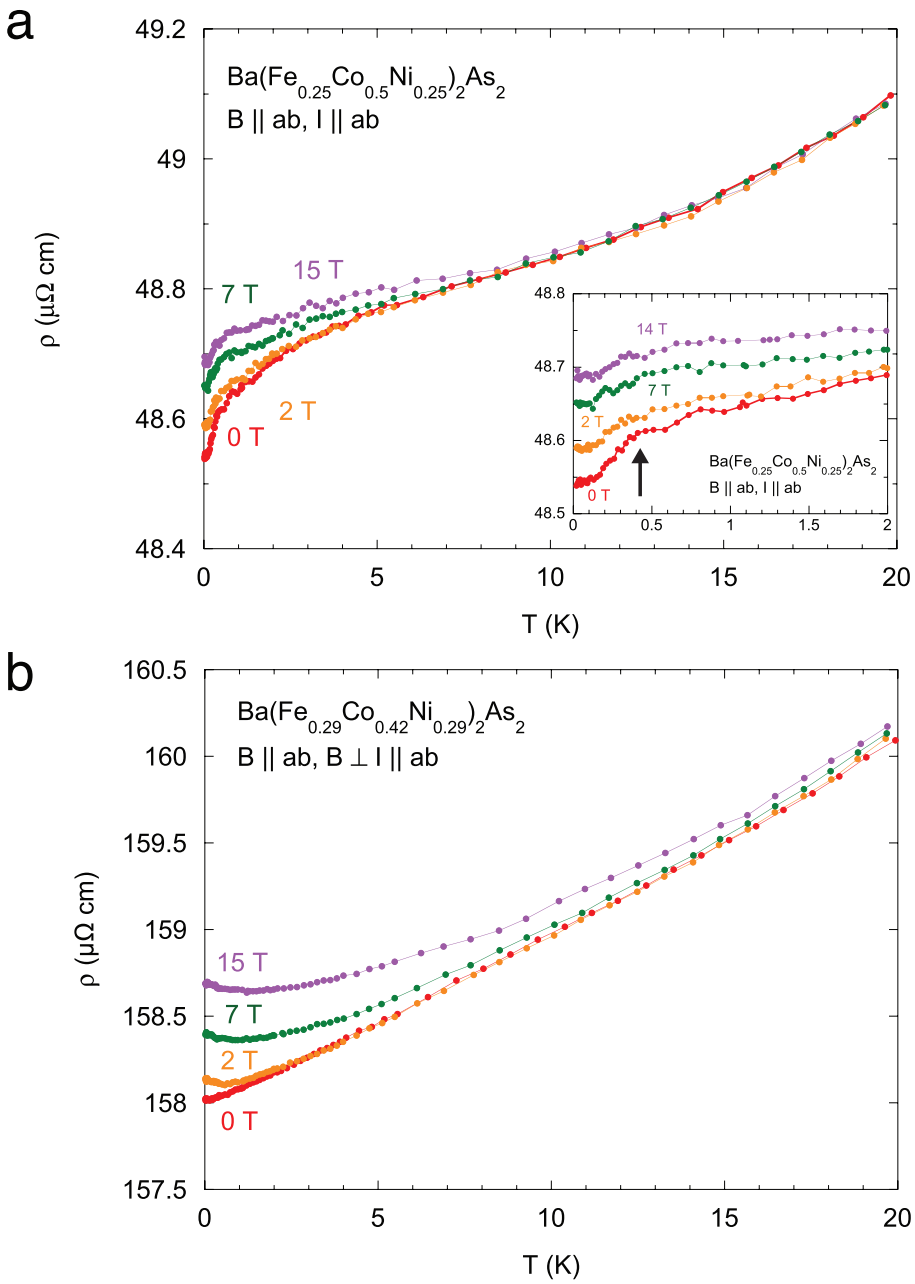

Supplementary Figure 9: **Resistivity for Ba(Fe,Co,Ni)$_2$As$_2$**. **a**, temperature dependence of resistivity for Ba(Fe$_{0.25}$Co$_{0.5}$Ni$_{0.25}$)$_2$As$_2$. A resistive kink possibly involving a phase transition is observed at 400 mK. The transition temperature is robust against applying field. **b**, temperature dependence of resistivity for Ba(Fe$_{0.29}$Co$_{0.42}$Ni$_{0.29}$)$_2$As$_2$, showing non-Fermi liquid behavior at zero field, diminished with magnetic field.

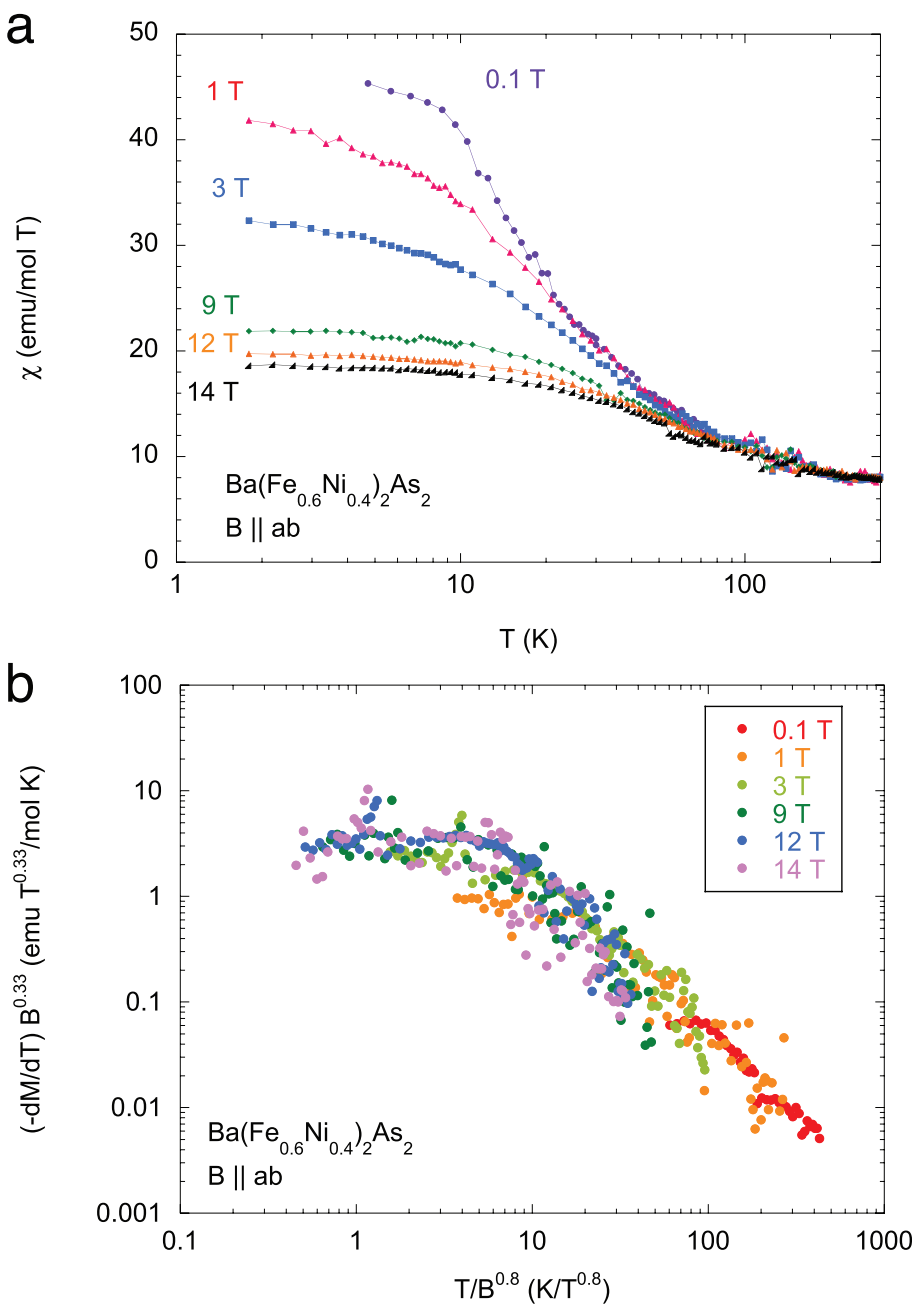

Supplementary Figure 10: **Quantum critical scaling in the magnetization for $Ba(Fe,Ni)_2As_2$.** **a**, Temperature dependence of the susceptibility χ for $Ba(Fe,Ni)_2As_2$ ($B \parallel ab$). Less diverging behavior in χ implies the system is located slightly far from the quantum critical point. **b**, Quantum critical scaling in the magnetization with critical exponents of $d/z = 2/3$ and $z/y_b = 0.8$, slightly different from those extracted in $Ba(Fe_{1/3}Co_{1/3}Ni_{1/3})_2As_2$.

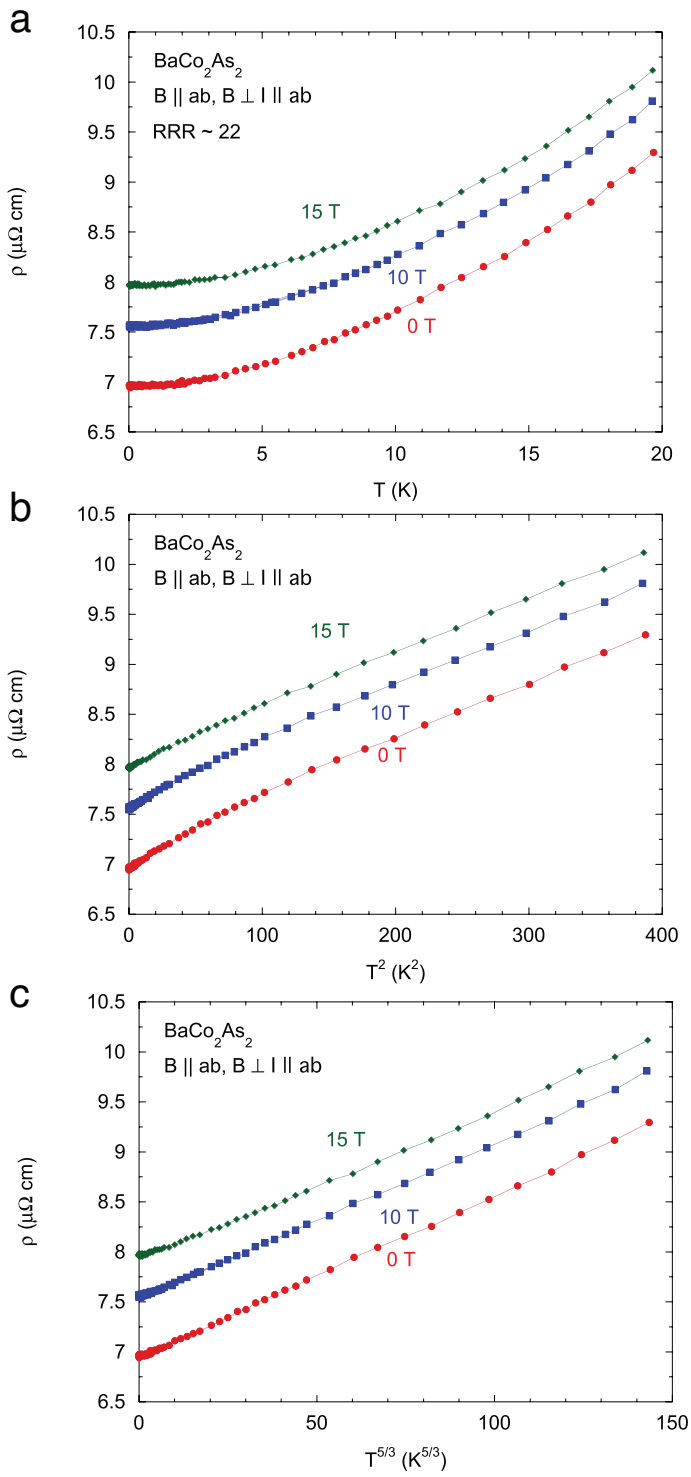

Supplementary Figure 11: **Ferromagnetic quantum critical scattering for $BaCo_2As_2$.** **a**, Temperature dependence of resistivity for $BaCo_2As_2$. The resistivity for $BaCo_2As_2$ as a function of **a**, T^2 and **b**, $T^{5/3}$, suggestive of ferromagnetic quantum critical scattering in 3D systems and reminiscent of marginal Fermi liquid $ZrZn_2$.

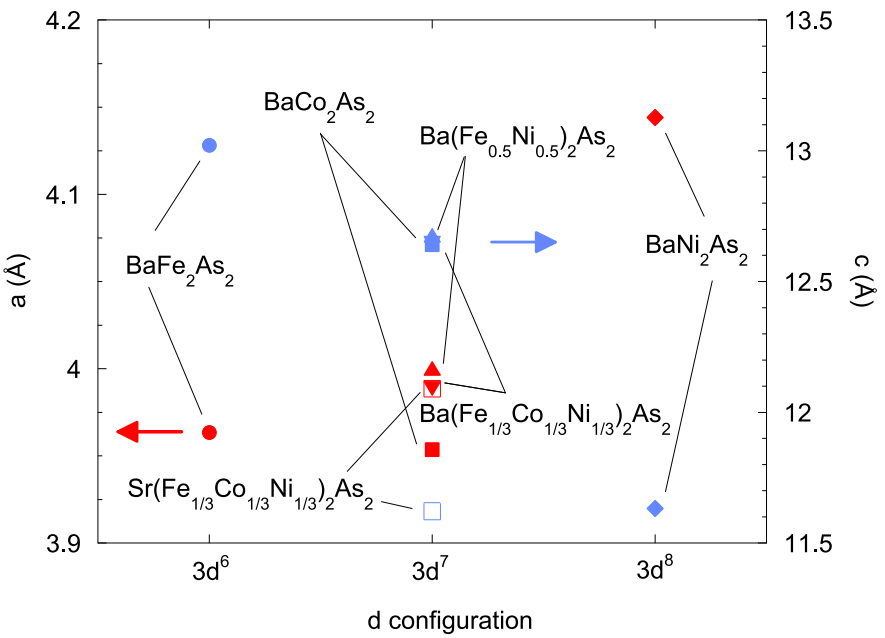

Supplementary Figure 12: Lattice constant of ATM_2As_2 (A = Ba, Sr, TM = Fe,Co,Ni). Lattice parameters a (red) and c (blue) as a function of $3d$ configurations for $BaFe_2As_2$ (•), $BaCo_2As_2$ (■), $Ba(Fe_{1/3}Co_{1/3}Ni_{1/3})_2As_2$ (▼), $Ba(Fe_{0.5}Ni_{0.5})_2As_2$ (▲), $BaNi_2As_2$ (♦), and $Sr(Fe_{1/3}Co_{1/3}Ni_{1/3})_2As_2$ (□).

SUPPLEMENTARY TABLES

Supplementary Table 1: Crystallographic data for $A(\mathbf{Fe}_{1/3}\mathbf{Co}_{1/3}\mathbf{Ni}_{1/3})_2\mathbf{As}_2$ (A = Ba, Sr) determined by single-crystal x-ray diffraction.

	Ba	Ba	Sr
Temperature	250 K	150 K	250 K
Structure	tetragonal	tetragonal	tetragonal
Space group	I4/mmm	I4/mmm	I4/mmm
a (Å)	3.9920(3)	3.9826(3)	3.9885(8)
c (Å)	12.6191(8)	12.6269(10)	11.621(5)
V (Å^3)	201.10(3)	200.28(3)	184.87(9)
Z (formula unit/unit cell)	2	2	2
R_1 ($I \geq 2\sigma(I)$)	0.0101	0.0112	0.0158
wR_2 (all data)	0.0251	0.0264	0.0344
Atomic coordinates (Wyckoff):			
Ba/Sr (2a)	0, 0, 0	0, 0, 0	0, 0, 0
Fe/Co/Ni (4d)	0.5, 0, 0.25	0.5, 0, 0.25	0.5, 0, 0.25
As (4e)	0.5, 0.5, 0.35160(3)	0.5, 0.5, 0.35171(3)	0.5, 0.5, 0.35840(7)
Isotropic displacement parameters U_{eq} (Å^2):			
Ba/Sr	0.01058(8)	0.00740(8)	0.0122(2)
Fe/Co/Ni	0.00961(10)	0.00681(10)	0.0133(2)
As	0.00913(9)	0.00649(9)	0.01224(19)
Bond lengths (Å):			
Ba/Sr-As	3.3875(3)	3.3818(3)	3.2653(7)
Fe/Co/Ni-As	2.3723(2)	2.3695(2)	2.3588(6)
Fe/Co/Ni-Fe/Co/Ni	2.8228(2)	2.8161(2)	2.8203(4)
Bond angles (deg):			
As-Fe/Co/Ni-As	114.575(16)	114.362(15)	115.44(4)
As-Fe/Co/Ni-As	106.981(7)	107.083(7)	106.57(2)

SUPPLEMENTARY NOTE 1: NON-FERMI LIQUID TO FERMI LIQUID CROSSOVER IN THE RESISTIVITY

The Non-Fermi liquid behavior in the temperature dependence of resistivity is strongly suppressed with magnetic field. Upon applying magnetic field, the recovery of Fermi liquid behavior, $\rho \propto T^2$, is observed, independent of applied magnetic field directions at low temperatures (Supplementary Figure 1a and b). The crossover temperature from non-Fermi liquid to Fermi liquid behavior, T_{FL}, is extracted from the deviation from T^2-fit.

SUPPLEMENTARY NOTE 2: ABSENCE OF MOOIJ CORRELATIONS AND VALIDITY OF THE MATTHIESSEN'S RULE

Transport properties in highly disordered metals show strong deviations from those described by the Boltzmann model. In the disordered metals, different scattering processes can no longer be treated independently, in other words, Matthiessen's rule breaks down. With introducing disorders, the residual resistivity in conventional metals increases toward the Mott-Ioofe-Regel limit, leading to a change of sign of the temperature coefficient of resistivity $d\rho/dT$ from positive to negative at high temperatures [2]. The sign change anticorrelates with the residual resistivity, known as Mooij correlations [3]. In the Mooij regime, polaronic renormalization of disorder plays an important role in the scattering mechanism, causing the breakdown of Matthiessen's rule.

On the other hand, in $Ba(Fe_{1/3}Co_{1/3}Ni_{1/3})_2As_2$, which can be considered as a highly disordered version of $BaCo_2As_2$, the introduction of disorder by counter-doping to Co sites enhances the residual resistivity, but causes no decrease in the slope of resistivity at high temperatures, resulting in a simple parallel shift of the resistivity (Supplementary Figure 2). This indicates the present system is not in the Mooij regime and allows us to extract inelastic scattering part using the Matthiessen's rule.

SUPPLEMENTARY NOTE 3: ISOTROPY OF NON-FERMI LIQUID BEHAVIOR AND $\Gamma(\mathbf{T},\mathbf{B})$ SCALING

Despite of the quasi layered structure, the non-Fermi-liquid magnetoresistance of $Ba(Fe_{1/3}Co_{1/3}Ni_{1/3})_2As_2$ is independent of applied field orientations. Supplementary Figure 3 shows the temperature dependence of resistivity in different applied field configurations. Independent of the applied field orientations, the quasi-T-linear dependence of resistivity at zero field is suppressed with field, suggesting the spatial dimensionality is three (fig.1e in the main text).

Obtaining from the magnetoresistance as shown in Supplementary Figure 3, we plot $\Gamma(T, B)$ scaling in the resistivity, independent of field directions with respect to the current direction. For the in-plane field orientations ($B \parallel ab$), either longitudinal ($B \parallel I$) or transverse magnetoresistance ($B \perp I$) provides the ratio of scaling parameters of $\eta = 0.55$ (Supplementary Figures 4a and b). By contrast, magnetoresistance in the perpendicular field orientation ($B \parallel c$) gives the ratio of $\eta = 0.67$ (Supplementary Figures 4c and d). The anisotropy of the scaling parameter ratio $\eta_{B\parallel ab}/\eta_{B\parallel c}$ is 0.82 and close to unity, suggesting isotropic scatterings. The non-Fermi liquid behavior in the magnetization measurements is also independent of applied field orientations, evidenced by the isotropy between the magnetization along $B \parallel c$ and $B \parallel ab$ (Supplementary Figure 5). The critical exponent of magnetization δ is 1.34, obtained by a fit to the data using $M \sim B^{\frac{1}{\delta}}$.

SUPPLEMENTARY NOTE 4: COMPARISON WITH MARGINAL FERMI LIQUID

The observed non-Fermi liquid like scattering rate ($\sim T$ in transport (fig.1a) or $\sim E$ in ARPES (fig.4d)) is evocative of the phenomenological marginal Fermi liquid model, where electronic specific heat and magnetic susceptibility shows logarithmic temperature dependence, $\sim a \ln(\lambda/T) + b$ [4]. While the marginal Fermi liquid form provides as good a fit to our susceptibility data below 10 K as $T^{-1/3}$ behavior does (Supplementary Figure 6a), it can be fitted to our specific heat data in the narrow temperature range only below 400 mK (Supplementary Figure 6b), yielding a worse fit than $C_e/T \sim T^{-0.25}$. Besides the fitting, considering the scaling for magnetization and specific heat derived from a single universal free energy, we conclude that the marginal Fermi liquid scenario does not appear to explain

our data well, compared to the quantum critical scaling.

SUPPLEMENTARY NOTE 5: KADOWAKI-WOODS RELATION

In Fermi liquids with strong electron correlations, including heavy fermion metals, the ratio of T^2-coefficient of temperature dependence of resistivity A and specific heat coefficient $\gamma = C_{\rm e}/T$ shows a universal value $A/\gamma^2 \sim a_{KW} = 10\ \mu\Omega$ cm mol^2 K^2 J^{-2}. As shown in Supplementary Figure 7, A/γ^2 for $Ba(Fe_{1/3}Co_{1/3}Ni_{1/3})_2As_2$ decreases with magnetic field, and approaches a_{KW}, supportive of recovering the Fermi liquid state by applying magnetic field.

SUPPLEMENTARY NOTE 5: QUANTUM CRITICAL SCALING

The quantum critical scaling observed in magnetization (fig. 2c) and specific heat (fig. 2d) implies the presence of universal function of T/B in the free energy. We can assume the generic form for the free energy F as,

$$F(B,T) = T^{\frac{d+z}{z}} \tilde{f}_F \left(\frac{B}{T^{y_b/z}} \right) = B^{\frac{d+z}{y_b}} f_F \left(\frac{T}{B^{z/y_b}} \right), \tag{S1}$$

where y_b is the scaling exponent related to magnetic field B, d is the spatial dimension, and z is the dynamical exponent. Assuming this form of free energy, we can derive magnetization $M = \partial F/\partial B$ and specific heat $C/T = -\partial^2 F/\partial T^2$. The magnetization is written by,

$$M = B^{(d+z)/y_b - 1} f_M \left(\frac{T}{B^{z/y_b}} \right), \tag{S2}$$

where the scaling function f_M is also a universal function of $x = T/B^{z/y_b}$, given by,

$$f_M(x) = [(d+z)/y_b] f_F(x) - (z/y_b) x f'_F(x). \tag{S3}$$

To extract the critical exponents, we obtain the derivative of M,

$$-\frac{dM}{dT} = B^{d/y_b - 1} f'_M \left(\frac{T}{B^{z/y_b}} \right). \tag{S4}$$

By comparing this with the scaling relation observed in fig. 2c, the critical exponents yield,

$$\begin{cases} d/y_b - 1 &= -1/3 \\ z/y_b &= 1. \end{cases} \tag{S5}$$

These equations provide

$$\begin{cases} z &= y_b \\ d/z &= 2/3. \end{cases} \tag{S6}$$

Likewise, the specific heat can be given by,

$$\frac{C(B,T)}{T} = -\frac{\partial^2 F}{\partial T^2} = T^{(d-z)/z} \tilde{f}_C \left(\frac{B}{T^{y_b/z}} \right), \tag{S7}$$

where $\tilde{f}_C(\tilde{x})$ is a scaling function of $\tilde{x} = B/T^{y_b/z}$,

$$\tilde{f}_C(\tilde{x}) = (d(d+z)/z^2)\tilde{f}_F(\tilde{x}) - (y_b(2d+z-y_b)/z^2)\tilde{x}\tilde{f}'_F(\tilde{x}) + (y_b^2/z^2)\tilde{x}^2\tilde{f}''_F(\tilde{x}) \tag{S8}$$

$$= (d(d+z)/z^2)\tilde{f}_F(0) + \tilde{g}_C(\tilde{x}), \tag{S9}$$

where, $\tilde{g}_C(\tilde{x})$ is field-dependent part of $\tilde{f}_C(\tilde{x})$. Using this expression, we can extract field dependent part of specific heat,

$$\frac{\Delta C_{\mathrm{e}}(B,T)}{T} = \frac{\Delta C_{\mathrm{e}}(B,T)}{T} - \frac{\Delta C_{\mathrm{e}}(0,T)}{T} = T^{\frac{d-z}{z}} \tilde{g}_C(B/T^{y_b/z}) = B^{\frac{d-z}{y_b}} g_C(T/B^{z/y_b}), \tag{S10}$$

where $g_C(x)$ is temperature-dependent part of $f_C(x)$. By comparing this with the scaling relation in fig. 2d, we obtain the critical exponents yielding,

$$\begin{cases} (d-z)/y_b &= -1/3 \\ z/y_b &= 1, \end{cases} \tag{S11}$$

also providing the same parameters as the eqs. (S6), namely,

$$\begin{cases} z &= y_b \\ d/z &= 2/3. \end{cases} \tag{S12}$$

SUPPLEMENTARY NOTE 6: SCALING FUNCTION AND FERMI TO NON-FERMI LIQUID CROSSOVER

The obtained scaling relations clearly show the Fermi to non-Fermi liquid crossover behavior. For $T/B \gg 1$, we observe non-Fermi liquid diverging behavior in the susceptibility, $\chi \propto T^{-1/3}$, implying $f_M(x) \propto x^{-1/3}$. On the other hand, in the other limit of $T/B \ll 1$, we observed temperature independent susceptibility, suggestive of the recovery of FL regime. From these observations, we can write the asymptotic forms of $f_M(x)$,

$$f_M(x) \propto \begin{cases} x^{-1/3} & T \gg B \text{ quantum critical regime} \\ const + O(x^2) & T \ll B \text{ Fermi liquid regime.} \end{cases} \tag{S13}$$

These asymptotic forms allow us to specify a universal function,

$$f_M(x) = c(x^2 + a^2)^{-1/6}, \tag{S14}$$

reproducing the behavior in $x \ll 1$ and $x \gg 1$ limits. Using eq. (S6),

$$M = cB^{2/3}(x^2 + a^2)^{-1/6}. \tag{S15}$$

The peak position in dM/dT gives the crossover temperature T^* by using $\frac{d}{dT}(dM/dT) = 0$, which gives,

$$T^*/B = x^* = \sqrt{3}a/2. \tag{S16}$$

Extracted from this equation, $T^*(B)$ is plotted in the phase diagram (fig. 3c).

Similarly, T^* can also be extracted from the scaling in the specific heat, which follows the Maxwell relation linking the entropy to the magnetization,

$$\frac{\partial S(B,T)}{\partial B} = \frac{\partial M(B,T)}{\partial T}. \tag{S17}$$

Integrating both sides with respect to B, we can obtain,

$$\int_0^B \frac{\partial S(B,T)}{\partial B} dB = \int_0^B \frac{\partial M(B,T)}{\partial T} dB. \tag{S18}$$

Since

$$\int_0^B \frac{\partial S(B,T)}{\partial B} dB = S(B,T) - S(0,T) = \int_0^T \frac{\Delta C_{\mathrm{e}}(B,T)}{T} dT, \tag{S19}$$

using eq.(S6), (S18), and (S19), we get,

$$\frac{\Delta C_{\mathrm{e}}(B,T)}{T} = \frac{\partial^2}{\partial T^2} \int_0^B M(B,T) dB = \int_0^B B^{-4/3} f''_M(x) dB, \tag{S20}$$

where

$$f''_M(x) = -\frac{c}{3}\left(x^2 + a^2\right)^{-7/6} \left[1 - \frac{7}{3}\frac{x^2}{x^2 + a^2}\right]. \tag{S21}$$

The peak positions in the scaling function of $\Delta C_{\mathrm{e}}/T$ obtained from a fit to the data give the crossover temperature $T^*(B)$, consistent with T^* from M as plotted in the phase diagram (fig. 3c).

SUPPLEMENTARY NOTE 8: TERNARY PHASE DIAGRAM AND POSSIBLE COMPETING PHASE

Supplementary Figure 8 shows a ternary phase diagram for $Ba(Fe,Co,Ni)_2As_2$ with red circles indicating the locations of $BaCo_2As_2$, $Ba(Fe_{0.25}Co_{0.5}Ni_{0.25})_2As_2$, $Ba(Fe_{0.29}Co_{0.42}Ni_{0.29})_2As_2$, $Ba(Fe_{1/3}Co_{1/3}Ni_{1/3})_2As_2$, and $Ba(Fe_{0.5}Ni_{0.5})_2As_2$. Determined by energy dispersion spectroscopy, the compositions of Fe, Co, and Ni allow the samples to hold $3d^7$ configuration. Interestingly, the very-low-temperature charge transport for $Ba(Fe_{0.25}Co_{0.5}Ni_{0.25})_2As_2$ reveals a resistive kink at 400 mK, possibly associated with a phase transition (Supplementary Figure 9a), robust against magnetic fields, while that for $Ba(Fe_{0.25}Co_{0.5}Ni_{0.25})_2As_2$ shows linear T behavior, suppressed with applying field (Supplementary Figure 9b).

Heavily electron doped $Ba(Fe,Ni)_2As_2$, assumedly sharing the same $3d^7$ configuration with $BaCo_2As_2$ and $Ba(Fe_{1/3}Co_{1/3}Ni_{1/3})_2As_2$, also shows non-Fermi liquid behavior in the magnetic susceptibility. As shown in Supplementary Figure 10a, the susceptibility divergently increases with decreasing temperatures, followed by the saturation below 10 K even at $B = 0$ T. This saturation at finite temperatures implies $Ba(Fe,Ni)_2As_2$ is located slightly away from a QCP. The non-Fermi liquid temperature dependence is strongly suppressed with applying magnetic field, indicative of the recovery of Fermi liquid regime at the applied field of 14 T. Similar to $Ba(Fe_{1/3}Co_{1/3}Ni_{1/3})_2As_2$, the crossover from Fermi liquid to non-Fermi liquid indeed allows the quantum critical scaling in the magnetization with the critical exponents of $d/z = 2/3$ and $z/y_b = 0.8$ (Supplementary Figure 10b), while the obtained z/y_b is slightly different from that for $Ba(Fe_{1/3}Co_{1/3}Ni_{1/3})_2As_2$.

SUPPLEMENTARY NOTE 9: QUANTUM CRITICAL FERROMAGNETIC SCATTERINGS IN $BaCo_2As_2$

As evinced by the observation of the enhanced Wilson ratio and violation of the Koringa ratio, $BaCo_2As_2$ is located close to the ferromagnetic quantum instabilities. The instabilities actually cause unusual scatterings in the charge transport for $BaCo_2As_2$ (Supplementary Figure 11a). Unlike $Ba(Fe_{1/3}Co_{1/3}Ni_{1/3})_2As_2$, the temperature dependence of resistivity for $BaCo_2As_2$ is not sublinear, but superlinear. To clarify the exponent of the temperature

dependence, we plot the resistivity as a function of T^2 (Supplementary Figure 11b), expected for Fermi liquid, and of $T^{5/3}$ (Supplementary Figure 11c), expected for three dimensional quantum critical ferromagnets. Very similar to quantum critical ferromagnetic metal $ZrZn_2$ [5], the perfect linear-in-$T^{5/3}$ dependence of the resistivity below $T = 20$ K highlights the presence of abundant quantum critical scatterings in $BaCo_2As_2$, robust against applied field, even up to 15 T.

SUPPLEMENTARY NOTE 10: LATTICE CONSTANTS

The lattice constants a and c for $Ba(Fe_{1/3}Co_{1/3}Ni_{1/3})_2As_2$ were determined by x-ray diffraction with Cu-K_α radiation, plotted together with ATM_2As_2 (A =Sr and Ba, TM =Fe, Co and Ni) as a function of d configurations (Supplementary Figure 12). Sharing the same d configuration with each other, the lattice parameter c for $Ba(Fe_{1/3}Co_{1/3}Ni_{1/3})_2As_2$ is similar to those for $BaCo_2As_2$ and $Ba(Fe_{0.5}Ni_{0.5})_2As_2$, while a has a large variation by 1% among them.

SUPPLEMENTARY NOTE 11: SINGLE CRYSTAL REFINEMENTS

Single-crystal x-ray diffraction was performed at 150 K and 250 K for $Ba(Fe_{1/3}Co_{1/3}Ni_{1/3})_2As_2$ and at 250 K for $Sr(Fe_{1/3}Co_{1/3}Ni_{1/3})_2As_2$ with Bruker APEX-II CCD system equipped with a graphite monochromator and a MoKa sealed tube ($\lambda = 0.71073$ Å). The crystallographic data obtained from refinements for $Ba(Fe_{1/3}Co_{1/3}Ni_{1/3})_2As_2$ and $Sr(Fe_{1/3}Co_{1/3}Ni_{1/3})_2As_2$ are summarized in Supplementary Table 1. Note that the final indices of the refinements R_1 are 1.01 % (Ba at 250 K), 1.12 % (Ba at 150 K), and 1.58 % (Sr at 250 K), close to the best values for Ba 122 crystals [6], indicative of the high quality samples in which the doped transition metals are randomly distributed and do not form the clusters.

SUPPLEMENTARY REFERENCES

[1] Sefat, A. S. *et al.* Renormalized behavior and proximity of $BaCo_2As_2$ to a magnetic quantum critical point. *Phys. Rev. B* **79**, 024512 (2009).

[2] Lee, P. A. & Ramakrishnan, T. V. Disordered electronic systems. *Rev. Mod. Phys.* **57**, 287–337 (1985).

[3] Ciuchi, S., Di Sante, D., Dobrosavljević, V. & Fratini, S. The origin of mooij correlations in disordered metals. *npj Quantum Materials* **3**, 44 (2018).

[4] Varma, C. M., Littlewood, P. B., Schmitt-Rink, S., Abrahams, E. & Ruckenstein, A. E. Phenomenology of the normal state of Cu-O high-temperature superconductors. *Phys. Rev. Lett.* **63**, 1996–1999 (1989).

[5] Sutherland, M. *et al.* Transport and thermodynamic evidence for a marginal Fermi-liquid state in $ZrZn_2$. *Phys. Rev. B* **85**, 035118 (2012).

[6] Kirshenbaum, K. *et al.* Tuning magnetism in FeAs-based materials via a tetrahedral structure. *Phys. Rev. B* **86**, 060504 (2012).